Draft: 20 January 2013

Two LITTLE THINGS: DDO 133 and DDO 168 revealed

Dana Ficut-Vicas[1,2,5], Elias Brinks[1], Deidre Hunter[3], Bruce Elmegreen[4], Michael Rupen[5], Caroline Simpson[6], Fabian Walter[7], Se-Heon Oh[8,9], Adam Leroy[10], and LTTeam[11]

ABSTRACT

We present an analysis of the relationship between star formation rate (SFR) surface density and neutral gas surface density in two LITTLE THINGS dwarfs: DDO 133 and DDO 168. The H I data was observed with the National Radio Astronomy Observatory (NRAO) Very Large Array (VLA). We focus our interest on their SF characteristics extending current investigations of the Schmidt-Kennicutt law to the low luminosity, low metallicity regime. In both dwarfs, we find that SFR surface density relates with the atomic gas surface density. The tight correlation between the SFR surface density and the V band emission suggests that stars are playing an important role in enhancing the conditions necessary for H I to turn molecular. We confirm observationally the theoretical result which predicts that the $10\,\mathrm{M}_{\odot}\,\mathrm{pc}^{-2}$ threshold beyond which the gas turns molecular can have a higher value in dwarf galaxies. We find evidence that such a higher value for this threshold does not depend on metallicity alone. We discuss the applicability in dwarfs of a molecular gas predicting method based on the star formation efficiency (SFE) in spiral galaxies.

---

[1]Centre for Astrophysics Research, University of Hertfordshire, College Lane, Hatfield, AL10 9AB, UK; D.Vicas@herts.ac.uk, E.Brinks@herts.ac.uk

[2]Filiala Cluj-Napoca, Romanian Academy of Science, 19 Ciresilor, Cluj-Napoca, Romania

[3]Lowell Observatory, 1400 West Mars Hill Road, Flagstaff, Arizona, USA; dah@lowell.edu

[4]IBM Research Division, T.J Watson Research Centre, 1101 Kitchawan Road, Yorktown Hts., 10598, USA; bge@watson.ibm.com

[5]NRAO, Array Operations Centre, 1003 Lopezville Road, Socorro, NM 87801, USA; mrupen@aoc.nrao.edu

[6]Department of Physics, Florida International University, Miami, FL33199, USA; simpsonc@galaxy.fiu.edu

[7]Max-Planck Institut fur Astronomie, Konigstuhl, 17, D-69117, Heidelberg, Germany; walter@mpia-hd.mpg.de

[8]International Centre for Radio Astronomy Research, The University of Western Australia, 35 Stirling Hwy, Crawley, WA 6009, Australia; se-heon.oh@icrar.org

[9]ARC Centre of Excellence for All-sky Astrophysics (CAASTRO)

[10]National Radio Astronomy Observatory, 520 Edgemont Road, Charlottesville, VA 22903, USA;

[11]Everywhere

Subject headings: galaxies: dwarf — galaxies: irregular — galaxies: individual (DDO 133, DDO 168)

1. Introduction

Dwarf galaxies represent the dominant population of the universe by number, not only at present, but even more prominently so in the past. In terms of light contribution, their optical luminosity combined rivals the summed up luminosity of giant surface brightness galaxies (Mateo 1998). The advances made in technology reveal dwarfs to be more than simple systems of slow rotation, generally low densities and ultra slow evolution. Dwarf galaxies are the elementary composites of our universe. As the smallest Dark Matter (DM) dominated entities existing in the universe, they are essential to dark matter studies. Their low metallicity environments open a window on pristine environments, and hence are of interest for studying how star formation proceeds in chemically young systems.

Once it became established that massive star formation rates in irregular galaxies are comparable to those in spirals (Hunter et al. 1982) and spiral density waves are not necessary for forming massive stars (Elmegreen & Elmegreen 1986), dwarf irregulars came to be seen as interesting environments for investigating star formation mechanisms and triggers. Consequently, a multitude of questions arose such as how giant cloud complexes and stars form at all in sub-critical gas and to what extent turbulence contributes to SF in these environments (Struck & Smith 1999). Previous neutral hydrogen (H I) and optical observations of dwarf irregulars showed a better correlation between the star formation rate (SFR) and the V-band surface brightness than any other measure (Hunter et al. 1998; Hunter & Elmegreen 2004). Using a sample of spiral galaxies, Bigiel et al. (2008) found that there is no correlation between the H I surface density and SFR. More recently, however, when involving a sample of gas–rich dwarfs, Bigiel et al. (2010) find that just like in the outskirts of spiral galaxies, the star formation rate and neutral gas surface density do correlate in dwarfs. Are existing stars a more efficient predictor for SF than H I column density thresholds? What conditions need to be met for the neutral gas to turn molecular? What law, if any, dictates what fraction of neutral gas is converted into molecular gas?

To answer questions related to star formation in dwarfs, we initiated LITTLE THINGS (Local Irregulars That Trace Luminosity Extremes; Hunter et al. 2012), the successor of THINGS (The H I Nearby Galaxy Survey; Walter et al. 2008), a project that combines H I line maps, optical, ultraviolet and infrared data of 42 dwarf irregular galaxies. The LITTLE THINGS[12] candidates were selected to sample a wide range of luminosities, star formation rates and metallicities, yet are located near enough so that typical clouds, filaments and turbulent structures are resolved with

[12]http://www.lowell.edu/users/dah/littlethings/index.html

the Very Large Array[13] (VLA).

In this paper, we showcase LITTLE THINGS by presenting our findings on DDO 133 and DDO 168 (see Fig. 1). The two candidates have similar metallicities, a difference in V–band brightness of only one magnitude and also similar integrated star formation rates (see Table 1). These two dwarf galaxies have been observed at ultraviolet (Hunter et al. 2010), Hα (Hunter & Elmegreen 2004) and optical wavelengths (Hunter et al. 1982; Kennicutt et al. 2008; Hunter & Elmegreen 2006). DDO 133 is peculiar in the sense that whereas most of the major axis V–band profiles of dwarf galaxies are exponential (Hunter & Elmegreen 2006; Herrmann & LITTLE THINGS Team 2012), this galaxy's profile is flat. This galaxy has also been found to host a bar (Hunter & Elmegreen 2006). Neutral hydrogen in DDO 133 has been observed previously only with VLA D configuration but the data were never published. DDO 168, is classified as peculiar and noted to have a significant position angle difference between the optical and the H I attributed to a possible past disturbance. Its gas surface density drops a factor of 5.5 over the radius of the optical galaxy, but there is no reflection of such a drop in the optical colours. Broeils & van Woerden (1994) used the Westerbork Telescope for short (2 hours) observations sets of each of the 50 galaxies in their sample, including DDO 168. The peculiar H I spatial morphology of DDO 168 prompted deeper observations (Broeils & Rhee 1997), yet not at the resolution we are providing here. These new observations enabled them to describe DDO 168 as having a “symmetric distribution with a strong condensation towards the centre”.

In this paper we begin with Section 2 on observations, data reduction and imaging, continue with Section 3 on data presentation and Section 4 on star formation analysis fundamentals, methods used and preliminary results on the two dwarfs. Then we delve deeper into the subject of star formation in DDO 133 and DDO 168 in Section 5. We close with Section 6, the conclusions.

2. The Data

The LITTLE THINGS survey uses a multi–wavelength approach to investigate star formation in dwarf galaxies. The project combines young star tracers: Hα and *GALEX* ultraviolet images; old star tracers: $UBVJHK$ and *Spitzer* 3.6 and 4.5 μm images; dust tracers: *Spitzer* PACS 5.8 and 8.0 μm images, IRS spectra of H II regions, and MIPS 24, 70 and 160 μm images of dust emission. To trace clouds, filaments and turbulent structures that are important in star formation, the multi–wavelength domain is completed with H I data. The H I furthermore provides crucial

[13]The VLA is a facility of the National Radio Astronomy Observatory (NRAO). The NRAO is a facility of the National Science Foundation operated under cooperative agreement by Associated Universities, Inc. These data were taken during the upgrade of the VLA to the Expanded VLA or EVLA. In this paper we refer to the instrument as the VLA, the retrofitted antennae as EVLA antennae, and non-retrofitted antennae as VLA antennae. This emphasizes the hybrid nature of the instrument and distinguishes it from the far more powerful Jansky VLA or JVLA it has become since 2012.

information on the kinematics of the gas.

DDO 133 and DDO 168, were observed in VLA B, C and D array configurations (see Table 2). The following subsections give details on how the observations, data calibration, data combination and imaging were done for the two galaxies under study.

2.1. Observations, Data Reduction and Imaging

Our observations were scheduled while the Very Large Array (VLA) was going through its upgrade to Expanded Very Large Array (EVLA): the old VLA front–end and back–ends being replaced with new EVLA ones. Until the new correlator came online, to continue functioning the telescope relied on hardware to convert the digital signals from the EVLA front–end into analogue signals to be fed into the VLA correlator. This conversion however caused extra power to be aliased into the bottom 0.7 MHz of baseband, being strongest at the lowest frequencies and dropping off rapidly. The aliased signal manifests itself on EVLA–EVLA baselines as a noise increase, the correlator power entering with a quasi–random phase, thus scattering this aliased signal across the map. On VLA–EVLA baselines the signals are largely uncorrelated, leading to only a marginal noise increase. As the upgrade progressed however, the number of EVLA–EVLA baselines increased, leaving fewer reliable baselines to work with.

With the above issue in mind the observations were designed to make the best of the situation. The planning for observations followed a standard approach with a few extra measures which are mentioned in Hunter et al. (2012).

Both DDO 133 and DDO 168 have been observed in spectral line mode, in the B, C and D array configurations of the VLA. The time on source totals 22.6 hours for DDO 133 and 19.1 hours for DDO 168 (see Table 2). All observations were made by us from late 2007 through to 2008, with the exception of two D–array sets of DDO 133, which we took from the VLA archives. Whereas the archival observations were done in 2IF mode with online Hanning smoothing and 128 channels, for the new observations, taken during the VLA to EVLA transition we did not use online Hanning smoothing. In order to avoid phase jumps on EVLA–VLA baselines, we observed without Doppler tracking which was corrected for in the calibration stage. As a flux density and bandpass calibrator we used 3C286 for both sources (for more details, see Table 2). The secondary calibrator was chosen on the basis of brightness and proximity to the source. It was observed in scans of 4 minutes, alternating with every 20 minutes on source.

The final data set has 2.6 km s^{-1} velocity resolution for a total bandwidth of 1.56 MHz. For the data calibration and reduction we used the AIPS package. Standard routines were used, although extra steps were necessary to deal with the problems brought on by the VLA upgrade. Due to aliasing, we had to throw away the EVLA–EVLA baselines and due to the closure errors on EVLA–VLA baselines we had to also create a new average across the band, needed for calibration. The data reduction details can be found in Hunter et al. (2012).

To obtain the final data cube we use IMAGR in AIPS. However instead of doing a standard

CLEAN we opt for a Multi–Scale CLEAN (Cornwell 2008; Rich et al. 2008; Greisen et al. 2009). Standard IMAGR has difficulties dealing with extended structure: not only can it erroneously overestimate the flux by up to 50% (Jörsäter & van Moorsel 1995), neither can it reliably deal with the missing short spacings which are the ones collecting most of the signal in extended sources. We produce both natural and robust weighted cubes using the Multi–Scale CLEAN method (see Table 3). Detailed explanations regarding our approach and the deconvolution algorithm itself can again be found in Hunter et al. (2012).

Once the two galaxies were imaged we put them through a by now standard blanking process (Walter et al. 2008), where we discriminate against any regions which do not show emission above a set level in at least three consecutive channels. Through this method we create a master blanking cube based on the natural weighted maps smoothed to 25$''$ and blanked at 2σ or 2.5σ, which we further apply to all our cubes. Only then do we create the surface brightness (moment 0), velocity field (moment 1) and the velocity dispersion (moment 2) maps using the AIPS task XMOM. The H I surface brightness maps used in this paper are primary beam corrected using task PBCOR.

2.2. Ancillary Data

The *UBV* optical data of DDO 133 were obtained with the 1.1–m Hall telescope at Lowell Observatory, in January 2000. The *J*–band observations were undertaken in May 1998 again at Lowell Observatory with the 1.8–m diameter Perkins telescope. DDO 168 was observed with a similar setup, the 1.1–m Hall telescope for the *UBV* bands and 1.8–m Perkins telescope for the *JHK* bands, in 1999 and 1998. More details on the instrumental setup and data processing can be found in Hunter & Elmegreen (2006), where these data have been published. Hα data were taken from Hunter & Elmegreen (2004).

The FUV images used in this paper have been obtained by the Galaxy Evolution Explorer satellite (*GALEX*) which images simultaneously in two channels FUV (bandpass of 1350-1750 Å and resolution of 4$''$) and NUV (bandpass of 1750-2800 Å and resolution of 5$''$.6). The *GALEX* data processing details and analysis are presented in Hunter et al. (2010). The *Spitzer* data have been acquired as part of large surveys such as the SIRTF Nearby Galaxies Survey (SINGS; Kennicutt et al. 2003) and the Local Volume Legacy (LVL; Dale et al. 2009), which have been made available to the astronomical community as significant libraries of data on nearby galaxies in a multitude of bands, of which we use 3.6 μm and, 24 μm.

3. Data Presentation

3.1. Integrated Properties

We start by presenting the global H I profiles of DDO 133 on the left and DDO 168 on the right (Fig. 2), obtained by integrating the channel maps over the area of the source after subtracting the continuum background. The flux is given in Jansky and the channel separation for our data is 2.58 km s^{-1}. The channel maps are available in Appendix A, Fig. A1 and Fig. A2 respectively. The blue and red drawn lines represent our data, the robust and natural weighted cubes respectively. The dashed black line represents published single dish data from Springob et al. (2005) for DDO 133 and Hunter & Gallagher (1985) for DDO 168. Both DDO 133 and DDO 168 single dish observations were taken with the NRAO 43 m Green Bank telescope. The single dish data on DDO 168 were in a non–electronic version in units of brightness temperature, which we converted into flux measurements using a telescope gain of 3.3 Jy K^{-1} as given by van Zee et al. (1997).

On a channel by channel basis the robust cube agrees with the single dish measurements to within 20%, see Table 4. Discrepancies start to occur in DDO 168 where the shape of the single dish profile deviates somewhat from our data, most obviously in the velocity range of 200 to 250 km s^{-1}.

For DDO 133 we infer a systemic velocity of 331 ± 2 km s^{-1}. The total integrated flux is 36.42 Jy km s^{-1} corresponding to an H I mass of 1.05×10^8 M$_\odot$ (adopting a distance of 3.5 Mpc, see Table 4). We find this value to be in good agreement with a single dish measurement of 1.2×10^8 M$_\odot$ made with the NRAO 43 m Green Bank telescope (Fisher & Tully 1981). We are also within 10% agreement with the more recent single dish measurement from Springob et al. (2005).

For DDO 168, we measure a systemic velocity of 192 ± 3 km s^{-1}. The total integrated flux is 64 Jy km s^{-1} corresponding to an H I mass of 2.81×10^8 M$_\odot$, (adopting a distance of 4.3 Mpc, see Table 4). We again find this value in fair agreement with the single dish measurement of 77 Jy km s^{-1} made with the NRAO 43 m telescope (Hunter & Gallagher 1985) or the 76.5 Jy km s^{-1} value found by Huchtmeier & Richter (1986) with the Westerbork telescope.

3.2. Gas Distribution in DDO 133 and DDO 168

For both DDO 133 and DDO 168 we combine B, C and D array configuration VLA data into a master data set which probes high resolution structures as well as extended emission.

The H I in DDO 133 is organised in an extended moderately inclined disk with quite a number of holes (Fig. 3). When we further investigate the H I distribution map (see Fig. 4, top left), we find in close proximity to some of the holes two areas with dense H I. Neither of the two areas is central to the galaxy and in both areas the velocity dispersion is high (see Fig. 4, bottom right).

The H I gas is asymmetrical with respect to the optical disk. However the kinematical centre agrees well with the centre (gray plus in all panels of Fig. 3 and Fig. 4) indicated by the old stars traced by the *Spitzer* 3.6μm map and the optical data centre given by Hunter & Elmegreen (2006).

These authors based on an extensive V–band study find the galaxy to be barred, with the bar centre (RA: $12^{\rm h}\,32^{\rm m}\,54\overset{\rm s}{.}26$ and DEC: $31\,^{\circ}32'32\overset{''}{.}31$) offset from the galaxy centre (RA: $12^{\rm h}\,32^{\rm m}\,55\overset{\rm s}{.}40$ and DEC: $31\,^{\circ}32'14''$), a position angle difference of 8 °between the bar and the host galaxy and with a semi–major radius of 2.48 kpc, as determined by Hunter & Elmegreen (2006), and centered in what we marked with a circled gray plus in Fig. 5 and Fig. 3. In Fig. 5 we plot V band contours on top of the H I distribution map showing the twisting of the optical contours at the position of the proposed bar. The position of this feature matches one of the high H I concentrating areas we have previously mentioned.

The star formation regions as indicated in Fig. 3 follow the H I gas concentrations. Strong FUV and Hα emission is associated not only with the dense H I structure, but also with the rims of the most important H I holes. Compact FUV emission is found close to the edge of the H I holes, suggesting that we are witnessing the standard scenario of a supernova explosion creating a hole in H I and pushing material outwards, increasing the pressure on the rim of the H I hole and triggering new star formation there.

DDO 168, has a peculiar H I distribution confirming the results of Broeils & van Woerden (1994). The highest concentrations of H I lie in the centre of the galaxy but at a different orientation with regard to the optical bands peaks positions. In Fig. 5 we plot V–band contours on top of a map of the H I distribution and we notice that some of the contours deviate from an elliptical shape. These optical V–band contours match in position the region with the highest H I density. The centre of the optical disk, RA: $13^{\rm h}\,14^{\rm m}\,27\overset{\rm s}{.}20$ and DEC: $45\,^{\circ}55'46''$(marked with a gray plus in each panel of Fig. 7), given by Hunter & Elmegreen (2006), coincides with the kinematical centre indicated by the H I and the *Spitzer* 3.6 μm image. The velocity field (Fig. 6) of the H I gas also shows twisted isovelocity contours in the central part of the galaxy suggesting the presence of a bar, which however has not been confirmed in the V–band (Hunter & Elmegreen 2006) and is subject of further investigations in the following section.

In the case of DDO 168, we also find that the H I distribution is fairly symmetrical with respect to the optical images considered. Whereas the optical data suggest an inclined disk, where old stars and new stars coexist, where Hα and FUV tracers agree, the central neutral gas traced by the H I maps is obviously disrupted and misaligned with respect to the optical disk. Furthermore, another peculiarity of this system is the higher velocity dispersion compared to DDO 133. The velocity dispersion, is at its maximum (15 km s^{-1}) in the south-east part of the galaxy as indicated in the velocity dispersion map (see bottom right panel of Fig. 7). This feature, at least towards the centre of the galaxy could be easily be associated with dense H I and with the emission peaks in optical bands.

Although not aligned with it, the densest H I region in the centre of the galaxy is also where Hα and FUV peak (see Fig. 6) indicating the existence of young stars in those regions.

3.3. Kinematic study of DDO 133 and DDO 168

Our SF analysis depends on a kinematical analysis to provide the inclination of the galaxy under investigation.

We first extract various types of velocity fields of the galaxies from the natural–weighted cubes, the intensity–weighted mean (IWM), the single Gaussian fit and the hermite h_3 velocity fields. In particular, compared to the other types of velocity fields, the hermite h_3 velocity field using the Gauss–Hermite polynomial is able to model the skewness of a non–Gaussian velocity profile which is usually caused by multiple velocity components (van der Marel & Franx 1993). For this reason, it was adopted as the standard velocity field for the kinematic analyses of the THINGS galaxies sample (de Blok et al. 2008). We refer to Oh et al. (2008, 2011a) for more details and discussions.

The iso–velocity contours of the velocity fields (see Fig. 4 and Fig. 7) are distorted in some regions, which indicates the presence of non–circular motions in the galaxies. In general the small–scale distortions are mainly due to supernova–driven gas outflows or stellar winds in star–forming regions (Oh et al. 2011b). However, despite the distorted velocity fields, the circular rotation of the galaxies dominates the non–circular motions as shown by the overall rotation pattern in the velocity fields.

We derive the rotation curves of DDO 133 and DDO 168 by fitting a set of concentric tilted–rings to the hermite h_3 velocity fields of the galaxies, by means of the task ROTCUR in GIPSY (Begeman 1989). Each tilted–ring is characterised by six ring parameters: kinematic center (XPOS, YPOS), inclination INCL, position angle PA, expansion velocity VEXP, systemic velocity VSYS, and rotation velocity VROT (Begeman 1989). PA is measured counter–clockwise of the major axis of the receding half of a galaxy.

We fit tilted–ring models to the velocity fields and derive the final rotation curves of DDO 133 and DDO 168 as shown in the lower panels of Fig. 8 and Fig. 9. In the top two rows of both Fig. 8 and 9, the solid lines indicate the derived tilted–ring parameters that best describe the velocity fields. In addition, for reference, we also show the results (open circles) derived keeping all ring parameters free.

The resulting rotation velocities show a typical behavior: linearly increasing in the inner regions (solid–body) and only flattening in the outer regions. The maximum rotation velocities of DDO 133 and DDO 168 are $\sim$40 km s^{-1} around $\sim$4.0 kpc and $\sim$50 km s^{-1} around $\sim$2.5 kpc, respectively. In general, the shape of the rotation curves resembles those of THINGS dwarf galaxies with near–solid–body rotation in Oh et al. (2011a). As discussed in Bureau & Carignan (2002), the asymmetric drift correction is required for galaxies whose velocity dispersions are significant compared to their maximum rotation velocities. However, as shown in Fig. 4 and Fig. 7, the velocity dispersion maps of DDO 133 and DDO 168 show small velocity dispersions ($\sim$7 km s^{-1}) compared to their maximum rotation velocities ($\sim$40 km s^{-1} and $\sim$50 km s^{-1}), respectively. This implies that the pressure support in the disk is insignificant with respect to their circular rotation. We therefore ignore the asymmetric drift corrections for DDO 133 and DDO 168.

Although most ring parameters are well constrained, the inclination of DDO 133 shows a large scatter as a function of radius. We therefore examine the sensitivity of the rotation curves to the exact value of inclination by varying the inclination by +10 and -10 °as shown in panel (e) of Fig. 8. The rotation curves derived using these inclinations while keeping other ring parameters the same are indicated by the grey solid (for +10 °inclination) and dashed (for -10 °inclination) lines in Fig. 8(a). Despite large variations of the inclinations, the deviations of the resulting rotation velocities are insignificant ($\sim$5 km s^{-1}) with respect to the ones with the best–fit inclinations (i.e., black dots in the VROT panels of Fig. 8).

Applying the same ring parameters derived using the hermite h_3 velocity fields to the IWM and single Gaussian fit velocity fields, we also derive the IWM and single Gaussian fit rotation curves of the galaxies and compare them with the hermite h_3 rotation curves. As shown in Fig. 8(g) of DDO 133, the rotation curves derived using the different velocity fields are consistent with each other, suggestive of insignificant small–scale random non–circular motions in the galaxies.

When taking a closer look at the velocity field of DDO 133 one notices twisted iso–velocity contours which can be associated with the region indicated in V–band as hosting a bar (Hunter & Elmegreen 2006) although some can also be connected to the position of the H I holes in the neutral gas distribution map (see top left panel in Fig. 4). When it comes to confirming the V–band bar we find there is not enough kinematical evidence for its existence.

For DDO 168, the derived PA shows a gradual decrease towards the outer regions (see Fig. 9(b)) and this might be due to the presence of a bar in the galaxy. A bar feature in a dwarf galaxy is not uncommon, however bars are difficult to identify in irregular galaxies (Hunter & Elmegreen 2006). Even more so when taking in account that for these kind of galaxies, the bar may be offset to one side, as in the LMC (de Vaucouleurs & Freeman 1972) and/or the optical and gas kinematics do not agree on its existence, like the case of DDO 133 above and the case of NGC 2366 where the optical morphology suggest the presence of a bar, yet the the H I observations do not provide strong support for its existence (Hunter & Hoffman 1999; Hunter et al. 2001). More recent results by Kuzio de Naray et al. (2012) indicated that strong non-axisymmetry near the centre, most likely an end-on bar is hidden in the remarkably regular kinematics of NGC 6503. The evidence of a bar in the gas kinematics is related to non-circular motions associated with large scale symmetric deviations, where there is a major axis change in the inner parts (Bosma 1978, 1981). Such a major axis change will manifest itself in a position angle change with radius, misalignments of the major axis with other structures seen in the optical and non orthogonality of the major axis relative to the minor axis (Bosma 1981, 1996).

Besides, the PA change with radius mentioned earlier, DDO 168 clearly exhibits also a misalignment between the emission peaks in the optical and the radio data (see Fig. 6). When inspecting the PVD diagram along the major axis (see Fig. 9(i))and along the minor axis (see Fig. 9(j)) we are also able to confirm the non orthogonality of the major and minor axis. With such indications of the existence of a bar in the DDO 168 system, we attempt its kinematical confirmation, through modelling. In order to examine kinematically the possibility of the bar, we fit a flat disk model which includes a bar–like potential with a different PA but with the same inclination. Using the VELFIT developed by Spekkens & Sellwood (2007) we fit such a disk model to the hermite h_3 velocity field of DDO 168. The best fit of the model (see Fig. 9(h)) describes the disk of DDO 168 as a combination of a flat disk and a bar with the same inclination of 51 ° but different PAs of 261 ° and 327 °, respectively. Moreover, the lower reduced chi–squares value (χ^2_{red}) of the bisymmetric model with m = 2 perturbations than that of a flat disk model (see Fig. 9(g)) with m = 0 supports the idea that DDO 168 is better described by a model with a bar–like potential. As shown in panels (g) and (h) of Fig. 9, the best–fit bisymmetric model for DDO 168 shows considerable amounts of m = 2 perturbations that induce a larger ($\sim 10\,\mathrm{km\,s^{-1}}$) circular rotation velocity of the disk than that of the tilted–ring model. More details on the kinematics of DDO 168 can be found in Oh (2012, in prep.).

In conclusion, in our kinematical studies for DDO 168 we infer an inclination of 51 ° and also find evidence for the existence of a bar in this system. Although not photometrically confirmed, kinematically the bar indicated by the decrease of the PA angle with radius and the position velocity diagrams has been modelled with VELFIT and confirmed. With regard to DDO 133, we infer an inclination of 47 ° for this system and find no kinematical evidence to confirm the bar found in this system in previous *V*–band studies.

4. SF Analysis

In the field of star formation one important area of investigation is centered on the relationship between star formation rate density and gas density. It was Schmidt (1959) to first relate the star formation rate with the gas density through a power law, known as the Schmidt law. The gas density was represented at the time by atomic gas only. Later, Kennicutt (1989) using a sample of disk galaxies quantified the SFR using Hα as a tracer and related it to a gas density which for the first time also included molecular gas measurements. Of late, this area of research has evolved considerably as the number of SF tracers used has multiplied. While traditionally the SF law was studied as a globally averaged relationship (Kennicutt 1989, 1998), a more recent direction is investigating this relationship on a spatially resolved basis (Leroy et al. 2008; Bigiel et al. 2008, 2010; Leroy et al. 2012).

In our SF analysis we take the spatially resolved approach and use a diverse set of multi–wavelength data. Prior to the analysis we prepare our maps to ensure they have proper physical units, they are aligned and at the same resolution. We use the H I data as a reference for the alignment and convolution, mainly because the H I data have the lowest resolution among the considered wavelengths.

We can only speak of a SF law as long as we do not resolve individual star forming structures and each galaxy region we are considering is large enough to contain more than one phase of the star forming cycle (Onodera et al. 2010; Schruba et al. 2010). The working resolution has been chosen to be 400 pc linear resolution. This resolution takes into account the small size of dwarf galaxies, ensuring enough independent regions to be studied without reaching the anti–correlation scale where we find Giant Molecular Clouds (GMC) and no SF activity or SF regions and no GMCs. This resolution also allows comparison between the two galaxies presented here and also with other results in the literature. Both the FUV and the Hα maps have been corrected for foreground extinction using the Cardelli et al. (1989) extinction law and the Schlegel et al. (1998) colour index values. All plotted data are corrected for inclination.

We begin this section with a summary of common used star formation tracers, concisely describing what arguments and formulae have been employed in obtaining the star formation rate (SFR) surface density maps (see Section 4.1). Then we discuss how considerations regarding internal extinction (see Section 4.2) affect our SF plots. In Section 4.3 we compare the performance of the different tracers considered in the environment of the two chosen dwarfs and present some preliminary results. We describe their systematic effects in Section 4.4 where we explain in some detail the effects of inclination uncertainties to our results (see Section 4.4.1) and the effect of resolution on the SF plots (see Section 4.4.2).

4.1. SF tracers

The traditional star formation tracer is Hα, which is directly proportional to current massive SFR. The Hα emission traces massive, ionising stars, mainly grouped in OB associations. The conversion from Hα fluxes to SFRs was initially given by Kennicutt (1983, 1988). Later, Kennicutt (1998) improved on this relation and recently, Calzetti et al. (2007) reconsidered the IMF and the stellar population assumptions (model of a 100 Myr constant SFR versus the infinite age case assumed by Kennicutt 1998) and converged on the following relation:

$$\mathrm{SFR}[\mathrm{M}_\odot\,\mathrm{yr}^{-1}] = 5.3 \times 10^{-42}\, L^*_{H\alpha}[\mathrm{erg\ s}^{-1}] \tag{1}$$

where $L^*_{H\alpha}$ is the extinction corrected Hα luminosity. (Throughout this section the asterisk denotes that the luminosity or the flux has been corrected for internal extinction.)

Eq. 1 can be converted to SFR density as follows:

$$\Sigma_{\mathrm{SFR}}[\mathrm{M}_\odot\,\mathrm{yr}^{-1}\mathrm{kpc}^{-2}] = 6.34 \times 10^{2}\, I^*_{H\alpha}[\mathrm{erg\ s}^{-1}\ \mathrm{cm}^{-2}\ \mathrm{sr}^{-1}] \tag{2}$$

where $I^*_{H\alpha}$ is the extinction corrected flux density of the Hα emission.

The Hα emission however is to a certain extent affected by extinction. Estimates on internal extinction are based on measurements inside the Milky Way and more recently in the LMC and SMC (Gordon et al. 2003) and not on direct measurements. A way around this problem is by using dust measurements to estimate the obscured emission fraction. The dust heated by hot, massive stars emits at mid–infrared wavelengths such as that being observed by Spitzer at 24 μm and 8 μm. Whereas the 8 μm emission is sensitive to metallicity and star formation history, the 24 μm (in the absence of an AGN), is less affected by metallicity and the contribution of non–ionizing regions and can be used in combination with Hα to account for the dust obscured emission (Kennicutt et al. 2007). Calzetti et al. (2007) find a correlation between extinction corrected Pa$_\alpha$ and 24 μm emission which they used to correct Hα for dust extinction according to:

$$\mathrm{SFR}[\mathrm{M}_\odot\,\mathrm{yr}^{-1}] = 5.3 \times 10^{-42}\,(L_{H\alpha}[\mathrm{erg\,s}^{-1}] + (0.031 \pm 0.006)\, L_{24\,\mu\mathrm{m}}[\mathrm{erg\,s}^{-1}]) \tag{3}$$

Again expressed in units of surface density, this can be written as:

$$\Sigma_{\rm SFR}[{\rm M_\odot yr^{-1}\,kpc^{-2}}] = 6.34\times10^{2}\,I_{H\alpha}[{\rm erg\,s^{-1}\,cm^{-2}\,sr^{-1}}] + 0.246\times10^{-2}\,I_{24\,\mu{\rm m}}[{\rm MJy\,sr^{-1}}] \quad (4)$$

Salim et al. (2007), using a sample of 50 000 optically selected galaxies in the local universe, ranging from gas–rich dwarfs to massive ellipticals, find that for the star forming galaxies the SFRs obtained from UV–observations agree well with those obtained from measuring the Hα emission lines. Therefore the author proposes a SF tracer based on the FUV emission, which operates on a timescale of 100 Myr and directly probes the contribution of young, massive stars. Unfortunately, the FUV emission is heavily affected by internal extinction but as long as one is able to correct for that the FUV is a better SF tracer in the sense that it can probe further out in the galaxy than Hα (Meurer et al. 2004). Salim et al. (2007) empirically infer the conversion factor for a Salpeter IMF from stellar population modeling to the obscured SED combined with a transformation between Chabrier and Salpeter IMFs based on Bruzual & Charlot (2003) models and find:

$$\mathrm{SFR}[\mathrm{M_\odot\,yr^{-1}}] = 1.08\times10^{-28}\,L^*_{FUV}[\mathrm{erg\,sr^{-1}\,Hz^{-1}}] \quad (5)$$

where L^*_{FUV} represents the dust–corrected FUV luminosity.

Which expressed in terms of surface density becomes:

$$\Sigma_{\rm SFR}[{\rm M_\odot\,yr^{-1}\,kpc^{-2}}] = 8.1\times10^{-2}\,I^*_{FUV}[{\rm MJy\,sr^{-1}}] \quad (6)$$

where I^*_{FUV} is the extinction corrected FUV intensity.

Leroy et al. (2008) try to overcome the effect extinction has on the FUV emission by using 24 μm to infer the dust obscured component, in the same manner as Calzetti et al. (2007) had done for the Hα SFR calibration. They use the Salim et al. (2007) result, and take Eq. 6 as the unobscured FUV emission component and calibrate the second term which accounts for the dust obscured emission in two ways: by extrapolation from the term derived for Hα by Calzetti et al. (2007) and through direct estimates from comparing total SFR with FUV emission. They find:

$$\Sigma_{\rm SFR}[{\rm M_\odot\,yr^{-1}\,kpc^{-2}}] = 8.1\times10^{-2}\,I_{FUV}[{\rm MJy\,sr^{-1}}] + 3.2\times10^{-3}\,I_{24\,\mu{\rm m}}[{\rm MJy\,sr^{-1}}] \quad (7)$$

4.2. Internal Extinction

The above mentioned formulae are well established in spiral galaxies. However as we move to the lower metallicity regime the 24 μm emission becomes weaker, reflecting a lower dust content, and the FUV+24 μm and Hα+24 μm SF tracers become dominated by the noise in the 24 μm maps.

Recent studies (Gordon & Clayton 1998; Gordon et al. 2003) have shown that extinction is different from that found in the Milky Way in more metal poor environments such as the Large Magellanic Cloud (LMC) and Small Magellanic Cloud (SMC). Within the LMC, the reddening parameter $R_V = A_V/E(B-V)$ varies by 25% between the LMC average and the LMC2 supershell (Gordon et al. 2003). In the metal poor SMC, Gordon & Clayton (1998), have shown that the UV extinction curves in the actively star forming bar are linear with wavelength, rising more steeply than in the Milky Way, suggesting an even stronger extinction.

Hunter & Hoffman (1999), measure the Balmer decrement in H II regions in a sample of 39 dwarf irregular galaxies and find the internal reddening correction in H II regions is of 0.1 mag. They take half of this value to represent the layers outside the H II regions, thus an internal extinction colour index of 0.05 mag.

Because the dust contribution is small, applying a more radical UV extinction law as the one suggested for the SMC seemed in disagreement with the nature of the observed environment in both dwarfs. We have studied the effect of applying such an extinction law to our analysis and found that in the context of a low internal extinction colour index its effects on the SFR analysis are small compared to using the Milky Way extinction law.

If we adopt the Milky Way extinction law with $A_{H\alpha}$=2.5E(B-V) based on the Cardelli et al. (1989) extinction law and A_{FUV}=8.24E(B-V) from Wyder et al. (2007), the contribution to the SFR surface density of the internal extinction correction we apply to the FUV and Hα maps to account for the obscured emission should be equal to the contribution to the SFR surface density of the 24 μm emission we have measured. On this principle, in Fig. 10 we plot for both DDO 133 (top) and DDO 168 (bottom), SFR surface density based on FUV only points against SFR surface density based on FUV+24 μm (left) and SFR surface density based on Hα only points against SFR surface density based on Hα+24 μm (left), each colour representing a different internal extinction correction applied based on different colour index values. In red, for example, we represent the internal extinction colour index of 0.05 mag used in the literature. The black continuous line is marking a 1:1 relation between the two plotted quantities. The points with no internal extinction correction applied, in black, lie slightly above the continuous line, indicating that the 24 μm contribution to the SFR surface density map is minimal and that internal extinction is low. In this way we find that the best agreement with the 24 μm emission is obtained for internal FUV and Hα extinction corrections at the 1% level, both 10 times lower than the internal reddening correction measured in H II regions.

In conclusion, the internal extinction due to obscuration by dust particles that heated by UV photons emit in the 24 μm is minimal, therefore we choose to apply no internal extinction correction to our data.

4.3. Preliminary Results

In the Milky Way regime the formulae mentioned in Section 4.1 are well established, however as we move to the lower metallicity regime it becomes important to consider the metallicity dependence of the factors involved in these formulae (Calzetti et al. 2010). Metallicity affects the level of SFR by inducing a lower internal extinction and thus ionising radiation is able to penetrate deeper into dense clouds. As metallicity decreases, the 24 μm emission becomes shallower and its contribution to the FUV+24 μm and Hα+24 μm SF tracers is noise dominated. Consequently we chose to work with the FUV–only and the Hα–only SF tracers. In Fig. 11, the panels display SFR surface density versus H I surface density for both DDO 133 (top panels) and DDO 168 (bottom panels), where the SFR is derived from two different tracers, FUV only (left) and Hα only (right). As we can see in Fig. 11, the two chosen tracers agree well with each other in both galaxies. This agreement is expected since we are measuring the same quantity, the SFR, by involving two independent methods. The FUV only tracer has a good signal–to–noise which allows us to probe not only the higher end of the SF law but also the lower density regions (Lee et al. 2009). The Hα only tracer, although only sampling the higher end of the SFR law, is used for comparison.

The top panels in Figs. 12 and 13 show SFR surface density vs. H I surface density, where the SFR is derived from two different tracers, FUV only (top left) and Hα only (top right). The bottom panels we show the star formation efficiency (SFE) as a function of atomic gas surface density (bottom left) and stellar surface density (bottom right). In all panels we plot density contours, representing 10%,25%,50%,75% and 90% levels of the total density of points as the contour colour gets lighter. Both galaxies follow an ascending trend of the SFR with the increase in H I gas density.

Star formation efficiency (SFE) defined as the ratio between the SFR and gas surface densities is a measure of how much time is necessary for the existing gas to be consumed at the current SFR. We find this quantity to relate well with the atomic gas density, as in both galaxies the SFE follows an ascending trend with gas density (see Fig. 12 and Fig. 13 bottom left panels). When plotting SFE vs. stellar surface density inferred from the 3.6 μm map using a method described in Leroy et al. (2008), the relation between the two quantities is stronger for DDO 168 than for DDO 133.

4.4. Systematic effects

4.4.1. Inclination corrections and their contribution to the SF Plots

Attempts have been made to find their intrinsic shape, whether an oblate spheroidal like in spiral galaxies or a triaxial shape, by using the optical ratio between the minor and major axis (Hodge & Hitchcock 1966). Whereas van den Bergh (1988) argues that dwarfs are oblate spheroids with a thick disk (b/a=0.6) there are other authors (Binggeli & Popescu 1995) who argue that triaxiality is needed to describe the shape of dwarf irregulars and Blue Compact Dwarfs (BCDs). Another way to settle this argument is by measuring the ratio between the rotational velocity and the velocity dispersion of the stars. Ratios of V/σ in spiral galaxies range from 2 to 5 (Bottema 1993) implying a thin cold disk. The ratio of the LMC (van der Marel et al. 2002) equals 3, which lies within the range of spiral galaxies. There are not many stellar kinematics measurements for dwarfs, and those which exist are sampling the higher luminosity end, so this result might not be generally true for all dwarf irregulars (Hunter et al. 2005).

Adding to the difficult problem of establishing the true shape of our targets, more complications arise from the fact that in the dwarf regime the thin disk assumption doesn't necessary apply and one must also consider that the HI disk is thicker throughout a disk thickness correction is necessary. In this context de–projection becomes more challenging. In addition to the H I disk thickness, Banerjee et al. (2011) using a small sample of four dwarf galaxies where gas and stars gravitationally dominate the disk, found that most dwarf galaxies exhibit H I flaring with radius, in other words an exponential increase of the scale height with radius.

For the purpose of this paper to follow the simplest case scenario and disregard the galaxy shape assumptions, the H I disk thickness and the scale height component and only consider for de–projection the inclination corrections. The inclination is derived through kinematical studies, explained in detail in paragraph 3.2.

We considered separately how uncertainty in determining the inclination affects our SF analysis. In Fig. 14, we plot SFR density versus H I surface density for DDO 168 with two different inclination corrections applied. A higher inclination correction, red points, moves all points in the plot downward and leftward. Although the points position in the plot change with different inclination corrections the relationship between them remains the same. It is that relationship that constitutes the SF law we are interested in investigating, thus any inclination uncertainties do not affect our conclusions.

4.4.2. Resolution effect on the SF plots and its implications

Our radio interferometric data have larger beams than the optical, ultraviolet or even near and mid infrared data. In our SF analysis the resolution that the radio data imposes, never reaches the SF law break–up resolution, allowing a discussion on SF laws even when working at the highest available resolution. However if one convolves the data to a lower resolution the signal to noise improves and as shown in Fig. 15 the scatter reduces. For this reason we have adopted a common linear resolution of 400 pc, which also allows us to make comparisons between the two considered galaxies and the literature (Bigiel et al. 2008, 2010; Leroy et al. 2008). We have also considered a common linear resolution of 750 pc to further investigate the effects of resolution on the SF plots. As a general trend we can see that the decrease in resolution moves the points of the SF plot downwards and leftwards, see Fig. 15. This trend can be explained by simply considering the mathematics that goes into the convolution process. When one smoothes the data, the way the total flux is spread out in the map changes and the flux peak inside a beam element becomes smaller proportionally with the beam size increase. Thus, the change in resolution has an effect on the scatter, on the number of points, on the position of points in the SF plot, but not on the relationship between the points in the plot.

DDO 133 follows the general trend very closely, yet in the 750 pc resolution the group of points that fail to follow the main trend present in the 210 pc and 400 pc resolutions disappears. We explain this feature as deriving from the resolution degradation. The lower the resolution the less detail is preserved of the fine structure in the H I gas and FUV maps, thus that particular group of points associated with the finer structure is also lost in the smoothing process.

5. Discussion

5.1. Results in the Literature context

To describe how efficiently gas is turned into stars, Schmidt (1959) used a power law to relate the volume density of the interstellar neutral gas in a region of the Galaxy with the number of stars formed there per unit time and volume. Estimating total gas volume densities wasn't in any way trivial, therefore only when Buat et al. (1989) suggested using surface densities instead of volume densities that this direction of research started flourishing. This relation, $\Sigma_{SFR} \propto (\Sigma_{gas})^N$ was called the Star Formation law (SF law) or the Kennicutt-Schmidt law (K-S law), acknowledging the extensive work done by Kennicutt R. in this field. Although the power law form of the SF law originated from a logical association between the number of stars observed and the gas, the fuel available for forming them, there are physical reasons to expect such a relationship. For an individual giant molecular cloud (GMC) the power law index $N \approx 0.75$, whereas for a uniform population of GMCs $N \approx 0.75$ (Krumholz & McKee 2005). Further if the determining SF process is gravitational instability in the total gas with a constant scale height then $N \approx 1.4$, whereas if it is fundamentally collisional $N \approx 2$ (Bigiel et al. 2008). These theoretical expectations are in the range of the observationally derived values. Kennicutt (1989, 1998) find that when relating globally the SFR and the total gas for normal spirals $N \approx 2.47 \pm 0.39$ and for a mixt sample of galaxies $N \approx 1.40 \pm 0.15$. Kennicutt et al. (2007) observes in the galaxy NGC 5194 a strong correlation between the SFR and molecular gas surface densities and no significant correlation with the atomic gas surface density. Bigiel et al. (2008), using a large sample of THINGS spiral galaxies conclude that there is no relationship between the SFR and the H I surface densities, but rather a one to one relationship between the SFR surface density and the molecular gas surface density. Blanc et al. (2009) uses integral field unit (IFU) spectroscopy to map again NGC 5194 and confirms the results of Bigiel et al. (2008) regarding the SF law slopes and the strong correlation between SFR and molecular gas surface densities. As the astronomical community interest starts shifting towards more extreme environments, such as the ones in dwarfs, a close match is found between THINGS dwarfs and the outskirts of spiral galaxies (Bigiel et al. 2010). They prove that in the outskirts of nearby galaxies, spirals and dwarfs, there is a clear relationship between H I and star formation, moreover different parts of galaxies populate the $\Sigma_{SFR} - \Sigma_{gas}$ parameter space in their own way (Bigiel et al. 2011).

In Fig. 16, last panel we show the relationship between H I surface density and SFR surface density for DDO 133 and DDO 168 combined, relationship which we have previously discussed for each individual galaxy in the preliminary results Section (see Section 4.3). We find that the ascending trend of the SFR with the increase in H I gas density is followed in both galaxies. To quantify this correlation we use the Spearman's rank correlation coefficient, a measure of the statistical dependance between the ranks of two variables. Nonparametric or rank correlation is more reliable than the linear correlation (Press et al. 1992), as ranking ensures a perfectly known distribution function, in contrast with the not necessarily known probability function associated with the linear correlation coefficient. The Spearman's rank correlation ranges between -1 and 1, where

1 represents a perfect correlation, -1 a perfect anti–correlation and 0 means the two variables are completely uncorrelated. Whereas, for Bigiel et al. (2008) the H I used to infer the gas surface density map and the FUV used as a SF tracer to obtain the SFR map have a Spearman's correlation rank of 0.7, we find that the same correlation rank for DDO 133 and DDO 168 is 0.78 and 0.91 respectively, indicating a strong correlation between the SFR and H I surface densities. The correlation is stronger in DDO 168 than in DDO 133, because in DDO 133 we have a group of points that follow a rather different trend. We will talk more about those regions in Section 5.2.

Further we compare our results with the literature by attaching two panels that summarise the results of Bigiel et al. (2008, 2010) next to our own results (see Fig. 16). Our colour density contours show the galaxies in their entirety without the segregation based on r_{25} used by Bigiel et al. (2010). For both our galaxies, DDO 133 especially, we have very deep observations in the FUV and that becomes obvious in the figure when even with a more conservative cutoff of 5σ we are able to go deeper than the 3σ FUV sensitivity level represented by the horizontal dashed line in the Bigiel et al. (2010) plots shown in two of the panels of Fig. 16. We find that in all regions inside our two galaxies, the H I correlates with the FUV. Further, to estimate the functional relation between SFR and H I surface densities, in the distribution of points representing both DDO 133 and DDO 168, we use one of the linear regression methods: the ordinary least squares (OLS) Bisector, as recommended by Isobe et al. (1990). We find that $\Sigma_{SFR} \propto (\Sigma_{HI})^{1.8}$, a power law index number close to the 1.7 value found by Bigiel et al. (2010). The neutral gas depletion times, the inverse of the star formation efficiency, for both DDO 133 and DDO 168 range between 10^{10} yr and 3×10^{11} yr (see Fig. 12 and Fig. 13, bottom left panels), again similar to the Bigiel et al. (2010) results.

The THINGS dwarfs sample contains some sources that for a number of reasons (see Bigiel et al. (2008)) can be considered as intermediaries between spirals and dwarfs. Our results although consistent with theirs show what probing deeper into the extreme environment of dwarfs can do. Not only the H I vs. SFR relationship gets stronger, but also unexpected features surface. One of them is the high H I surface density end of $\sim 30\,M_\odot\,pc^{-2}$ in DDO 168, which goes beyond the $10\,M_\odot\,pc^{-2}$, the limit beyond which the H I turns molecular in normal metallicity galaxies (Bigiel et al. 2008). This not a systematic effect due to either resolution or inclination uncertainties. Only an extreme and unrealistic inclination correction could bring down the H I surface density value maxima in DDO 168 below that $10\,M_\odot\,pc^{-2}$ threshold (see Fig. 14). Similar, yet more radical ($\Sigma_{HI} \sim 100\,M_\odot\,pc^{-2}$) behaviour has been noted in the SMC by Bolatto et al. (2011). The magnitude of the effect in the SMC is attributed to the complex geometry of the source, which properly accounted for would decrease this above mentioned value by a factor of 1.5 – 2. This geometry corrected value is still beyond the $10\,M_\odot\,pc^{-2}$ limit. Although still preliminary, there are results which predict that the $10\,M_\odot\,pc^{-2}$ limit is inversely proportional with metallicity (Fumagalli et al. 2010; Krumholz et al. 2011). Such a relation would explain the geometry corrected value of the Σ_{HI} upper limit found for SMC and would predict for DDO 168, based on a metallicity: 12+log(O/H) = 8.29, a Σ_{HI} upper limit of $\sim 23\,M_\odot\,pc^{-2}$, 20% less than the value we observe. This 20% difference could be due to the gas distribution in DDO 168 combined with the uncertainties in the metallicity measurements. However, DDO 133 with a metallicity 12+log(O/H) = 8.23, slightly lower than the one in DDO 168, does not break the $10\,\mathrm{M}_{\odot}\,\mathrm{pc}^{-2}$ Σ_{HI} upper limit. This peculiar contradiction between the behaviour of the two galaxies can only be settled by exploring a larger sample. For this purpose in Fig. 17 we investigate further the relationship between metallicity and H I maxima, not only for our two dwarfs but also for the THINGS dwarfs. We find that at 400 pc linear resolution, there are also THINGS dwarfs such as DDO 63, DDO 53, DDO 50, NGC 2366, NGC 4214 which break the $10\,\mathrm{M}_{\odot}\,\mathrm{pc}^{-2}$ limit. The effect, although well contained to a $25\,\mathrm{M}_{\odot}\,\mathrm{pc}^{-2}$ limit, is there even in Bigiel et al. (2010) SFR vs H I surface densities plot. Comparing our data on DDO 133 and DDO 168 with the THINGS data on a number of 7 dwarfs we do not find any strong evidence for the predicted trend with metallicity. Consequently, there must be more parameters influencing the Σ_{HI} upper limit, than metallicity alone. Krumholz et al. (2009) shows that besides metallicity, the degree of clumping in gas also plays a role in the value of the H I maxima and one can imagine that the H I maxima variation from dwarf to dwarf could also be due to the particular phase of the star formation cycle that the dwarf galaxy is going through at the moment of observation. Both DDO 133 and DDO 168 have extended FUV emission throughout the galaxy, however the $H\alpha$ emission follows the FUV emission contours with more fidelity in DDO 168 than in DDO 133 (see Fig. 3 and Fig. 6). This suggests that while DDO 133 seems to go through a more quiescent stage, DDO 168 is presently actively forming stars. Massive star formation, such as the one traced by $H\alpha$ is more likely to happen in gas with high column densities. Roychowdhury et al. (2011) based on a sample of 23 extreme dwarfs find that the higher the $\Sigma_{SFR(H\alpha)}/\Sigma_{SFR(FUV)}$ ratio the more likely to find gas with a column density higher than the $10\,\mathrm{M}_{\odot}\,\mathrm{pc}^{-2}$ limit, a result we are also confirming here.

Another literature result that we compare our findings with is the following: dwarf irregulars show a better correlation between the star formation rate (SFR) and the V band surface brightness than any other measure (Hunter et al. 1998; Hunter & Elmegreen 2004). For this purpose we plot in Fig. 18 the SFR versus V–band emission (top right) for DDO 133 (black) and DDO 168 (red) and we find that the relationship between the two quantities is tighter (less scatter) than the relationship between SFR and H I gas density (top left). To asses the strength of the correlation between SFR and V–band surface densities we compute the Spearman's rank correlation coefficient and find: $r_s = 0.90$ for DDO 133 and $r_s = 0.92$ for DDO 168. Moreover we confirm the result existent in the literature and show that this relation holds not only globally but also on a pixel by pixel basis.

In the same figure, Fig. 18 we also plot SFR versus V–band emission (in red) and 3.6 μm emission (navy) for DDO 133 (bottom left) and SFR versus V–band emission (in red), K–band emission (orange) and 3.6 μm emission (navy) for DDO 168 (bottom right), to compare in what way does the SFR relate with the existent stars. Whereas the V–band is dominated by main sequence (MS) stars with a considerable contribution from red giants, the K–band is dominated by K giant stars and old stars. We only have K–band data available for DDO 168. When K–band maps are unavailable, 3.6 μm can be used as a proxy for the old stellar populations (Oh et al. 2008). The relationship persist at all considered wavelengths, but the relation to the V band remains tightest. For DDO 133 the correlation between SFR and the 3.6 μm emission ($r_s = 0.78$) has similar strength with the one between SFR and H I surface densities. For DDO 168 the correlations between SFR and the 3.6 μm emission ($r_s = 0.86$) and the K–band ($r_s = 0.78$) are both weaker than the one between SFR and H I surface densities. The optical and NIR bands follow each other very closely pointing towards a common ascending trend with the increase in SFR. Since they trace such different populations of stars, their agreement suggests that in these dwarf galaxies where dust contribution is minimal, the dominating population in all these bands is one and the same: old stars. Consequently it seems that in dwarfs such as DDO 133 and DDO 168 the V–band map traces the stellar surface density with the same fidelity as K–band or 3.6 μm maps. Thus the observed relationship of the SFR and the V– band surface densities is induced by the role played by existing stars. Stars act as local gas density enhancers and in turn the gas density sets the rate of molecular gas formation and in this way related to SFR.

Shi et al. (2011) find a correlation between SFE and stellar mass density, by looking at the dependance of Σ_{SFR} on Σ_{gas} and Σ_{star}. In terms of SFE, DDO 168 shows as expected, an ascending trend with the increase of stellar surface density (see Fig. 13, bottom right panel), whereas DDO 133 is rather ambiguous (see Fig. 12, bottom right panel). The inconsistency in the case of DDO 133 may be due to the 3.6 μm emission which is very weak. Further, Shi et al. (2011) explain this correlation as an indication of the critical role played by existing stellar populations in the current SF events. The role of existing stars in star formation in dwarf galaxies can be related to induced star formation, as well as to pressure-regulated molecular gas formation. According to the first scenario newly formed stars blow holes, rearrange the gas and influence the local gas density and trigger more cloud formation (Dolphin & Hunter 1998). The latter scenario however is believed to be also behind the relationship between molecular gas mass and K–band luminosity found by Leroy et al. (2005): the larger the K–band luminosity the higher the midplane hydrostatic pressures leading to higher gas densities and more efficient molecular gas formation. In DDO 133 for example there are clear indications of induced SF, whereas in the more compact DDO 168 the second scenario seems more probable. In conclusion, we cannot rule against any of the gas density enhancement mechanisms described above, but rather have indications that both mechanisms play their role at different moments in the life of a galaxy.

5.2. Multiple components in the SF Laws

We now turn our attention to the features emerging in the SFR and the H I surface densities relationship in DDO 133, features which suggest a multiple component SF Law. In Fig. 19, top left panel, a group of points that deviate from the main trend are found to be associated with particular regions in the neutral gas distribution map. Therefore we colour coded different significant regions in the neutral gas distribution map: red for H I shells regions, orange for high H I surface density regions and blue for the outskirts. In Fig. 19, using this particular colour code, we plot the position of the points on top of the highest resolution FUV (top right), H I (middle right) and Hα (bottom right) maps as well as display them in plots presenting SFE and SFR vs H I surface density and SFR surface densities. V band emission. We find that the abnormally sitting points (in red) represent the regions with H I shells. Most studies (Brinks & Bajaja 1986; Bagetakos et al. 2011) explain the creation of H I shells through star formation and their results are backed up by a correlation between small shells and OB associations. In a dwarf galaxy environment with no shear or spiral arms, the life of an H I hole is longer, so one cannot rule out the possibility of the H I hole outliving the star formation tracers that could have testified for that past SF event.

In our case, the smaller shells, in the central part of the galaxy are also associated with higher velocity dispersion components and of Hα and FUV emission. The presence of the Hα emission, the clumpy distribution of the FUV emission and the shell size suggest a rather recent SF event in these regions. However the bigger northern H I shell can only be associated with diffuse FUV emission, testifying to a considerably older SF episode. If we look at the bottom left panel of Fig. 19, we see that there is V band light in these regions, which betrays the presence of main sequence stars and to some extent a contribution from red giants. The stars that now contribute to the V–band, FUV and Hα emission when forming have created the H I shells. The remaining neutral gas is getting reorganised somewhere else, most likely enhancing the gas density at the shell edge, where a new generation of stars will be born in the future. In this induced SF scenario (Dolphin & Hunter 1998), the H I shells testify to where the SF sites were and not necessarily where they will be in the future. The 400 pc resolution element is able to pick up this fine detail in the SF cycle and it appears as a distinct feature in the SFR vs. H I surface densities plot (SF plot). If you look back at Fig. 15 where we compare how resolution influences our SF plot, you will find that the higher the value of the resolution element the smaller the number of points representing the shell region and the more diminished its effect on the overall trend of the SF plot. However, if the shell size is bigger than the resolution element than we are reaching a new kind of anti–correlation scale, one where in the chosen resolution element we have SF activity but no neutral gas to continue the SF cycle. In other words, the extra component of the SF law, corresponding to the H I shell regions it's not a true trend, but one artificially induced by reaching the anti–correlation scale.

In dwarf galaxies, because in their environment shells are able to grow unhindered reaching over 1 kpc in size, the shell regime is justifiably present in the pixel by pixel SF plots. If the shell regime feature is not properly accounted for, the choice of resolution element becomes difficult and galaxy dependent. However if its contribution to the SF plot is removed, the quest for a SF law can continue even at 400 pc resolution but only for the points which do not break any anti–correlation scale. In our case, if we remove the red points from the distribution of points considered in the Spearman's rank correlation coefficient computation for DDO 133, this coefficient changes its value from $r_s = 0.78$ to $r_s = 0.89$, a value closely matching with the one we find in DDO 168.

If we also look in Fig. 19, in the middle left panel at the way the star formation efficiency (SFE) evolves as a function of H I surface density, we find that meanwhile the galaxy tends to form more stars as the H I gas density is larger, the H I shell regions seem to have a constant SFE. This constancy in SFE should be interpreted rather as a quiescence state of those regions, where the FUV emission produced in the past SF episode is not related to the amount of gas that remained inside the shell.

5.3. Total gas determinations. Molecular gas predictions

Stars form out of molecular gas, therefore relating the SFR to the H I surface density is valuable only in the sense of studying the transition of atomic gas into molecular gas. In fact, Bigiel et al. (2010) has shown that such a relationship exists only in dwarfs and outskirts of spirals. This indirect relationship between the star formation process and the neutral gas behaviour has became more interesting since Bigiel et al. (2008) has proved that the SFR follows the molecules. Leroy et al. (2008) have investigated this relationship further and found the SFE of the molecular gas to be a constant: $\mathrm{SFE(H_2)} = 5.25 \times 10^{-10}\,\mathrm{yr^{-1}}$. This result based on CO observations of THINGS spiral and gas-rich dwarf galaxies can be used as a tool to predict the molecular gas quantity in galaxies where CO observations are not available.

We cannot directly observe H_2, we can only infer this quantity from CO observations (Schuster et al. 2007; Leroy et al. 2007b) and more recently from gas–to–dust ratios (Leroy et al. 2007a, 2011). Dwarf galaxies are low metallicity environments, where the CO molecules are under–abundant and thus cannot be used as proxies for molecular gas mass determinations (Bolatto et al. 2008; Leroy et al. 2007b). Therefore for dwarfs such as DDO 133 and DDO 168, once we acknowledge the fact that SFR in molecules does not depend on metallicity, in the sense that metallicity influences the CO and the total gas quantities do but not the H_2 quantity (Krumholz et al. 2009, 2011), we can use the Leroy et al. (2008) prediction to infer the molecular gas mass. We find a predicted amount of molecular gas of 1[illegible] $\times 10^7\,\mathrm{M_\odot}$ for DDO 133 and $1.8 \times 10^7\,\mathrm{M_\odot}$ for DDO 168. With a similar metallicity as our two dwarfs, in the SMC, Leroy et al. (2007a) have found the H_2 mass to be $3.2 \times 10^7\,\mathrm{M_\odot}$, a value which shows that our predicted values are well within the range of values estimated from CO and dust observations.

With a molecular gas estimation at hand, in order to derive the total gas mass, we correct by a factor of 1.34 to take into account the helium fraction and we obtain a value of $1.41 \times 10^8\,\mathrm{M_\odot}$ for DDO 133 and $3.71 \times 10^8\,\mathrm{M_\odot}$ for DDO 168. We use an empirical conversion to transform the 3.6 μm map intensity to K band intensity and from there using the K band mass to light ratio we obtain the stellar density map (Leroy et al. 2008). We then use this stellar density map to compute the stellar mass of DDO 133: $\mathrm{M_*} = 1.01 \times 10^8\,\mathrm{M_\odot}$ and of DDO 168: $\mathrm{M_*} = 2.02 \times 10^8\,\mathrm{M_\odot}$. For DDO 133, the mass of stars combined to the total gas mass yields a total baryonic mass of [illegible]3 $\times 10^8\,\mathrm{M_\odot}$, amounting to the [illegible] part of the dynamical mass $\mathrm{M_{dyn}} = 2.3 \times 10^9\,\mathrm{M_\odot}$ ($\mathrm{v_{max}}$=40 km s^{-1}, and $\mathrm{r_{max}}$=6.2 kpc). In turn, for DDO 168, the mass of stars combined to the total gas mass yields a total baryonic mass of $5.94 \times 10^8\,\mathrm{M_\odot}$, amounting to the [illegible] part of the dynamical mass $\mathrm{M_{dyn}} = 2.44 \times 10^9\,\mathrm{M_\odot}$ ($\mathrm{v_{max}}$=50 km s^{-1}, and $\mathrm{r_{max}}$=4.2 kpc).

6. Conclusions

In this paper, we present an extensive investigation of SF laws in the low metallicity environment of dwarf galaxies: DDO 133 and DDO 168. We summarise our results as follows:

- We use 24 μm emission maps to evaluate the internal extinction in the two dwarfs and find that it is minimal and no internal extinction correction is necessary for the SF analysis.

- In both DDO 133 and DDO 168 we find a relationship between SFR surface density and H I surface density. Although not a one–to–one relationship, the relationship we find matches previous results in the literature (Bigiel et al. 2010) in both H I surface density range and SFR surface density range.

- We are also able to confirm that the relationship between SFR surface density and V band luminosity (Hunter & Elmegreen 2004) is present also in the two galaxies studied. Moreover we find this relationship to be tighter than the one between SFR vs. H I surface density not only globally but also at the smaller scale level.

- The $10\,M_\odot\,pc^{-2}$ threshold, beyond which the gas turns molecular (Bigiel et al. 2008) has a different value in DDO 168. Indeed when taking into account the metallicity, the theoretically predicted (Krumholz et al. 2009) threshold for DDO 168 matched the observed within 20%. In the case of DDO 133, however, although its metallicity is similar to the one in DDO 168 the threshold does not increase beyond the well known $10\,M_\odot\,pc^{-2}$. We conclude that metallicity alone cannot explain why in DDO 168 the H I maxima goes beyond the $10\,M_\odot\,pc^{-2}$ threshold.

- At 400 pc resolution DDO 133 shows ageing stars in H I holes as distinct features on the Kennicutt–Schmidt plot. While most of the points in this SFR vs. H I surface density plot follow the same trend as in DDO 168, there is a group of points that stand out as different from the main trend points. We isolated those points and found they correspond to areas in the galaxy where we have H I shells. Because the H I shells are regions with SF activity but no gas for continuing the SF cycle, once the resolution element of the Kennicutt–Schmidt plot is smaller then the size of the H I shell a new neutral anti-correlation scale is reached. Considering that in dwarfs the shell sizes can be over 1 kpc, we suggest disregarding the shell regions when investigating the relationship between SFR surface density and H I surface density.

- We discuss the applicability of the molecular gas prediction given by Leroy et al. (2008) to dwarf galaxies and find that as the SFR dependancy on molecular gas does not vary with metallicity (Krumholz et al. 2011), we can successfully estimate the amount of molecular gas in both our dwarf galaxies.

We thank the astronomy department of the University of Hertfordshire, for granting a doctoral scholarship to DF. We thank all the people at the National Radio Astronomy Observatory (NRAO) for all their help and support. A special thanks to Eric Greisen who invested time and patience in helping us tune Multi–Scale CLEAN for our project. We also thank Jeff Mangum and his team, and Dale Frail at NRAO who enriched the knowledge of DF by granting her an NRAO graduate internship. We thank the National Science Foundation (NSF) for the support that enabled the completion of this project through grants AST-0707563, AST-0707426, AST-0707468, and AST-0707835. This research has made use of the NASA/IPAC Extragalactic Database (NED) which is operated by the Jet Propulsion Laboratory, California Institute of Technology, under contract with the National Aeronautics and Space Administration.

Facilities: NRAO (VLA), SSC (*Spitzer* IRS,IRAC, MIPS), NASA (*GALEX*), CARLyon (HyperLEDA), NASA (NED).

REFERENCES

Bagetakos, I., Brinks, E., Walter, F., de Blok, W. J. G., Usero, A., Leroy, A. K., Rich, J. W., & Kennicutt, Jr., R. C. 2011, AJ, 141, 23

Banerjee, A., Jog, C. J., Brinks, E., & Bagetakos, I. 2011, MNRAS, 415, 687

Begeman, K. G. 1989, A&A, 223, 47

Bigiel, F., Leroy, A., & Walter, F. 2011, in IAU Symposium, Vol. 270, Computational Star Formation, ed. J. Alves, B. G. Elmegreen, J. M. Girart, & V. Trimble, 327–334

Bigiel, F., Leroy, A., Walter, F., Blitz, L., Brinks, E., de Blok, W. J. G., & Madore, B. 2010, ArXiv e-prints

Bigiel, F., Leroy, A., Walter, F., Brinks, E., de Blok, W. J. G., Madore, B., & Thornley, M. D. 2008, AJ, 136, 2846

Binggeli, B., & Popescu, C. C. 1995, A&A, 298, 63

Blanc, G. A., Heiderman, A., Gebhardt, K., Evans, II, N. J., & Adams, J. 2009, ApJ, 704, 842

Bolatto, A. D., Leroy, A. K., Rosolowsky, E., Walter, F., & Blitz, L. 2008, in IAU Symposium, Vol. 255, IAU Symposium, ed. L. K. Hunt, S. Madden, & R. Schneider, 274–277

Bolatto, A. D., et al. 2011, ApJ, 741, 12

Bosma, A. 1978, PhD thesis, PhD Thesis, Groningen Univ., (1978)

—. 1981, AJ, 86, 1825

Bosma, A. 1996, in Astronomical Society of the Pacific Conference Series, Vol. 91, IAU Colloq. 157: Barred Galaxies, ed. R. Buta, D. A. Crocker, & B. G. Elmegreen, 132

Bottema, R. 1993, A&A, 275, 16

Brinks, E., & Bajaja, E. 1986, A&A, 169, 14

Broeils, A. H., & Rhee, M. 1997, A&A, 324, 877

Broeils, A. H., & van Woerden, H. 1994, A&AS, 107, 129

Bruzual, G., & Charlot, S. 2003, MNRAS, 344, 1000

Buat, V., Deharveng, J. M., & Donas, J. 1989, A&A, 223, 42

Bureau, M., & Carignan, C. 2002, AJ, 123, 1316

Calzetti, D., et al. 2007, ApJ, 666, 870

—. 2010, ApJ, 714, 1256

Cardelli, J. A., Clayton, G. C., & Mathis, J. S. 1989, ApJ, 345, 245

Cornwell, T. J. 2008, IEEE Journal of Selected Topics in Signal Processing, 2, 793

Dale, D. A., et al. 2009, ApJ, 703, 517

de Blok, W. J. G., Walter, F., Brinks, E., Trachternach, C., Oh, S.-H., & Kennicutt, Jr., R. C. 2008, AJ, 136, 2648

de Vaucouleurs, G., & Freeman, K. C. 1972, Vistas in Astronomy, 14, 163

Dolphin, A. E., & Hunter, D. A. 1998, AJ, 116, 1275

Elmegreen, B. G., & Elmegreen, D. M. 1986, ApJ, 311, 554

Fisher, J. R., & Tully, R. B. 1981, ApJS, 47, 139

Fumagalli, M., Krumholz, M. R., & Hunt, L. K. 2010, ApJ, 722, 919

Gordon, K. D., & Clayton, G. C. 1998, ApJ, 500, 816

Gordon, K. D., Clayton, G. C., Misselt, K. A., Landolt, A. U., & Wolff, M. J. 2003, ApJ, 594, 279

Greisen, E. W., Spekkens, K., & van Moorsel, G. A. 2009, AJ, 137, 4718

Herrmann, K. A., & LITTLE THINGS Team. 2012, in American Astronomical Society Meeting Abstracts, Vol. 219, American Astronomical Society Meeting Abstracts #219, 106.05

Hodge, P. W., & Hitchcock, J. L. 1966, PASP, 78, 79

Huchtmeier, W. K., & Richter, O. G. 1986, A&AS, 63, 323

Hunter, D. A., & Elmegreen, B. G. 2004, AJ, 128, 2170

—. 2006, ApJS, 162, 49

Hunter, D. A., Elmegreen, B. G., & Baker, A. L. 1998, ApJ, 493, 595

Hunter, D. A., Elmegreen, B. G., & Ludka, B. C. 2010, AJ, 139, 447

Hunter, D. A., Elmegreen, B. G., & van Woerden, H. 2001, ApJ, 556, 773

Hunter, D. A., Gallagher, J. S., & Rautenkranz, D. 1982, ApJS, 49, 53

Hunter, D. A., & Gallagher, III, J. S. 1985, AJ, 90, 1789

Hunter, D. A., & Hoffman, L. 1999, AJ, 117, 2789

Hunter, D. A., Rubin, V. C., Swaters, R. A., Sparke, L. S., & Levine, S. E. 2005, ApJ, 634, 281

Hunter, D. A., et al. 2012, AJ, 144, 134

Isobe, T., Feigelson, E. D., Akritas, M. G., & Babu, G. J. 1990, ApJ, 364, 104

Jörsäter, S., & van Moorsel, G. A. 1995, AJ, 110, 2037

Karachentsev, I. D., et al. 2003, A&A, 398, 467

Kennicutt, Jr., R. C. 1983, ApJ, 272, 54

—. 1988, ApJ, 334, 144

—. 1989, ApJ, 344, 685

—. 1998, ApJ, 498, 541

Kennicutt, Jr., R. C., Lee, J. C., Funes, José G., S. J., Sakai, S., & Akiyama, S. 2008, ApJS, 178, 247

Kennicutt, Jr., R. C., et al. 2003, PASP, 115, 928

—. 2007, ApJ, 671, 333

Krumholz, M. R., Leroy, A. K., & McKee, C. F. 2011, ApJ, 731, 25

Krumholz, M. R., & McKee, C. F. 2005, ApJ, 630, 250

Krumholz, M. R., McKee, C. F., & Tumlinson, J. 2009, ApJ, 699, 850

Kuzio de Naray, R., Arsenault, C. A., Spekkens, K., Sellwood, J. A., McDonald, M., Simon, J. D., & Teuben, P. 2012, MNRAS, 427, 2523

Lee, J. C., et al. 2009, ApJ, 706, 599

Leroy, A., Bolatto, A., Stanimirovic, S., Mizuno, N., Israel, F., & Bot, C. 2007a, ApJ, 658, 1027

Leroy, A., Bolatto, A. D., Simon, J. D., & Blitz, L. 2005, ApJ, 625, 763

Leroy, A., Cannon, J., Walter, F., Bolatto, A., & Weiss, A. 2007b, ApJ, 663, 990

Leroy, A. K., Walter, F., Brinks, E., Bigiel, F., de Blok, W. J. G., Madore, B., & Thornley, M. D. 2008, AJ, 136, 2782

Leroy, A. K., et al. 2011, ApJ, 737, 12

—. 2012, AJ, 144, 3

Mateo, M. L. 1998, ARA&A, 36, 435

Meurer, G. R., Thilker, D., Bianchi, L., Ferguson, A., Madore, B., Gil de Paz, A., Hameed, S., & GALEX Science Team. 2004, in Bulletin of the American Astronomical Society, Vol. 36, American Astronomical Society Meeting Abstracts, 1410

Oh, S.-H., L. T. T. 2012, preprint (2012)

Oh, S.-H., Brook, C., Governato, F., Brinks, E., Mayer, L., de Blok, W. J. G., Brooks, A., & Walter, F. 2011a, AJ, 142, 24

Oh, S.-H., de Blok, W. J. G., Brinks, E., Walter, F., & Kennicutt, Jr., R. C. 2011b, AJ, 141, 193

Oh, S.-H., de Blok, W. J. G., Walter, F., Brinks, E., & Kennicutt, Jr., R. C. 2008, AJ, 136, 2761

Onodera, S., et al. 2010, ApJ, 722, L127

Press, W. H., Teukolsky, S. A., Vetterling, W. T., & Flannery, B. P. 1992, Numerical recipes in C. The art of scientific computing

Rich, J. W., de Blok, W. J. G., Cornwell, T. J., Brinks, E., Walter, F., Bagetakos, I., & Kennicutt, Jr., R. C. 2008, AJ, 136, 2897

Roychowdhury, S., Chengalur, J. N., Kaisin, S. S., Begum, A., & Karachentsev, I. D. 2011, MNRAS, 414, L55

Salim, S., et al. 2007, ApJS, 173, 267

Schlegel, D. J., Finkbeiner, D. P., & Davis, M. 1998, ApJ, 500, 525

Schmidt, M. 1959, ApJ, 129, 243

Schruba, A., Leroy, A. K., Walter, F., Sandstrom, K., & Rosolowsky, E. 2010, ApJ, 722, 1699

Schuster, K. F., Kramer, C., Hitschfeld, M., Garcia-Burillo, S., & Mookerjea, B. 2007, A&A, 461, 143

Shi, Y., Helou, G., Yan, L., Armus, L., Wu, Y., Papovich, C., & Stierwalt, S. 2011, ApJ, 733, 87

Spekkens, K., & Sellwood, J. A. 2007, ApJ, 664, 204

Springob, C. M., Haynes, M. P., Giovanelli, R., & Kent, B. R. 2005, ApJS, 160, 149

Struck, C., & Smith, D. C. 1999, ApJ, 527, 673

van den Bergh, S. 1988, PASP, 100, 344

van der Marel, R. P., Alves, D. R., Hardy, E., & Suntzeff, N. B. 2002, AJ, 124, 2639

van der Marel, R. P., & Franx, M. 1993, ApJ, 407, 525

van Zee, L., Maddalena, R. J., Haynes, M. P., Hogg, D. E., & Roberts, M. S. 1997, AJ, 113, 1638

Walter, F., Brinks, E., de Blok, W. J. G., Bigiel, F., Kennicutt, R. C., Thornley, M. D., & Leroy, A. 2008, AJ, 136, 2563

Wyder, T. K., et al. 2007, ApJS, 173, 293

This preprint was prepared with the AAS LaTeX macros v5.2.

Table 1: General Properties

Name	DDO 133	DDO 168
Alt. Name	UGC07698	UGC08320
RA (hh mm ss.s) [J2000]	12 32 55.4	13 14 27.9
DEC (dd mm ss.s) [J2000]	31 32 14.1	45 55 09.0
D[a] (Mpc)	3.5	4.3
R_H[b] (′)	2.33	2.32
m_B[c] (mag)	12.70	11.92
M_V[d] (mag)	-16	-15.27
(12+log(O/H))[e]	8.23	8.29
log (SFR_D)[f] ($M_\odot$ yr^{-1} kpc^{-2})	-2.93	-2.33

[a] Distance (taken from NED and Karachentsev et al. (2003))

[b] Holmberg radius measured to a B-band surface brightness of about 26.66 from Hunter & Elmegreen (2006)

[c] Apparent blue magnitude corrected for galactic extinction and extinction internal to the galaxy, from HyperLEDA

[d] Absolute V magnitude from Hunter & Elmegreen (2006)

[e] Metallicity from Hunter & Hoffman (1999)

[f] SFR from Hunter & Hoffman (1999) determined from $L_{H\alpha}$ divided by πR_D^2, where R_D is 1.12′ for DDO 133 and 0.66′ for DDO 168.

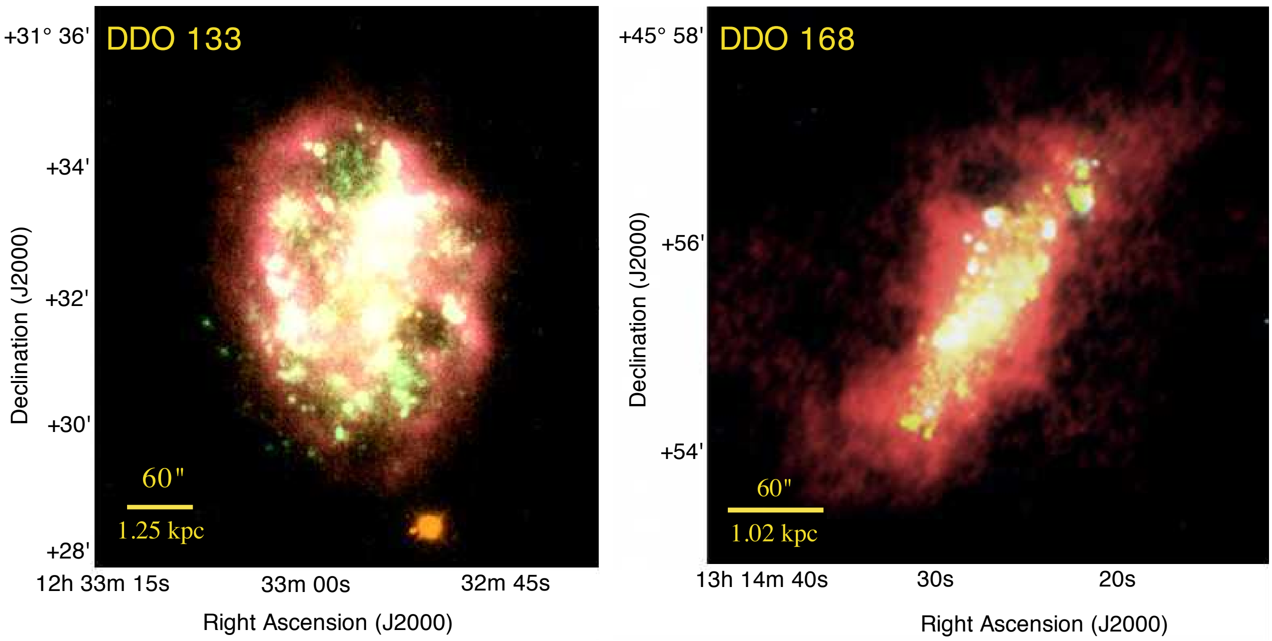

Fig. 1.— Composites of the H I map as red, FUV map as green and V image as orange for DDO 133 (left) and DDO 168 (right). North is at the top; east is to the left.

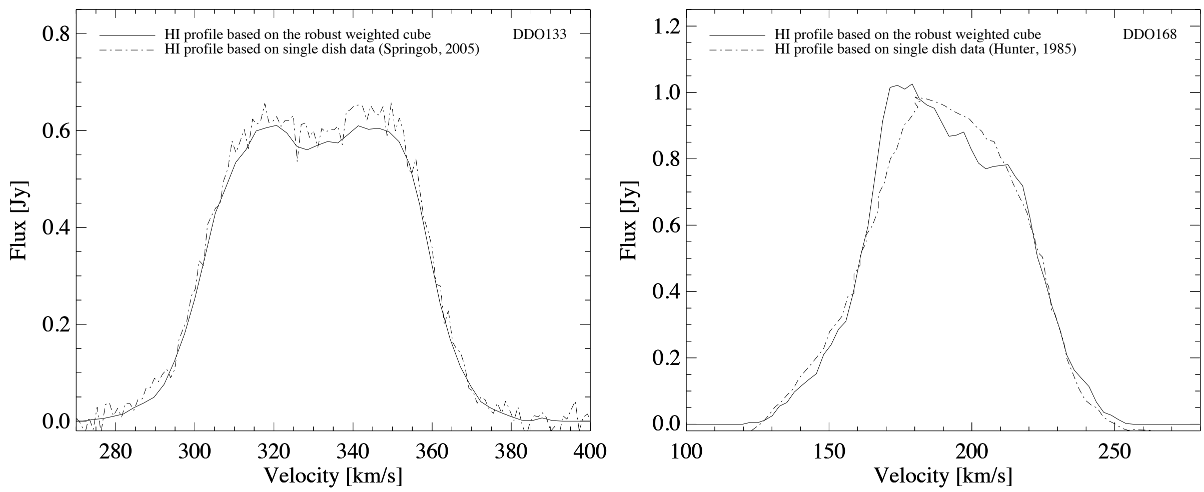

Fig. 2.— H I profiles of the calibrated, B, C, D array configurations combined, VLA data for DDO 133 (left) and DDO 168 (right), robust weighted (blue continuous line) compared with published single dish profiles (black dashed line).

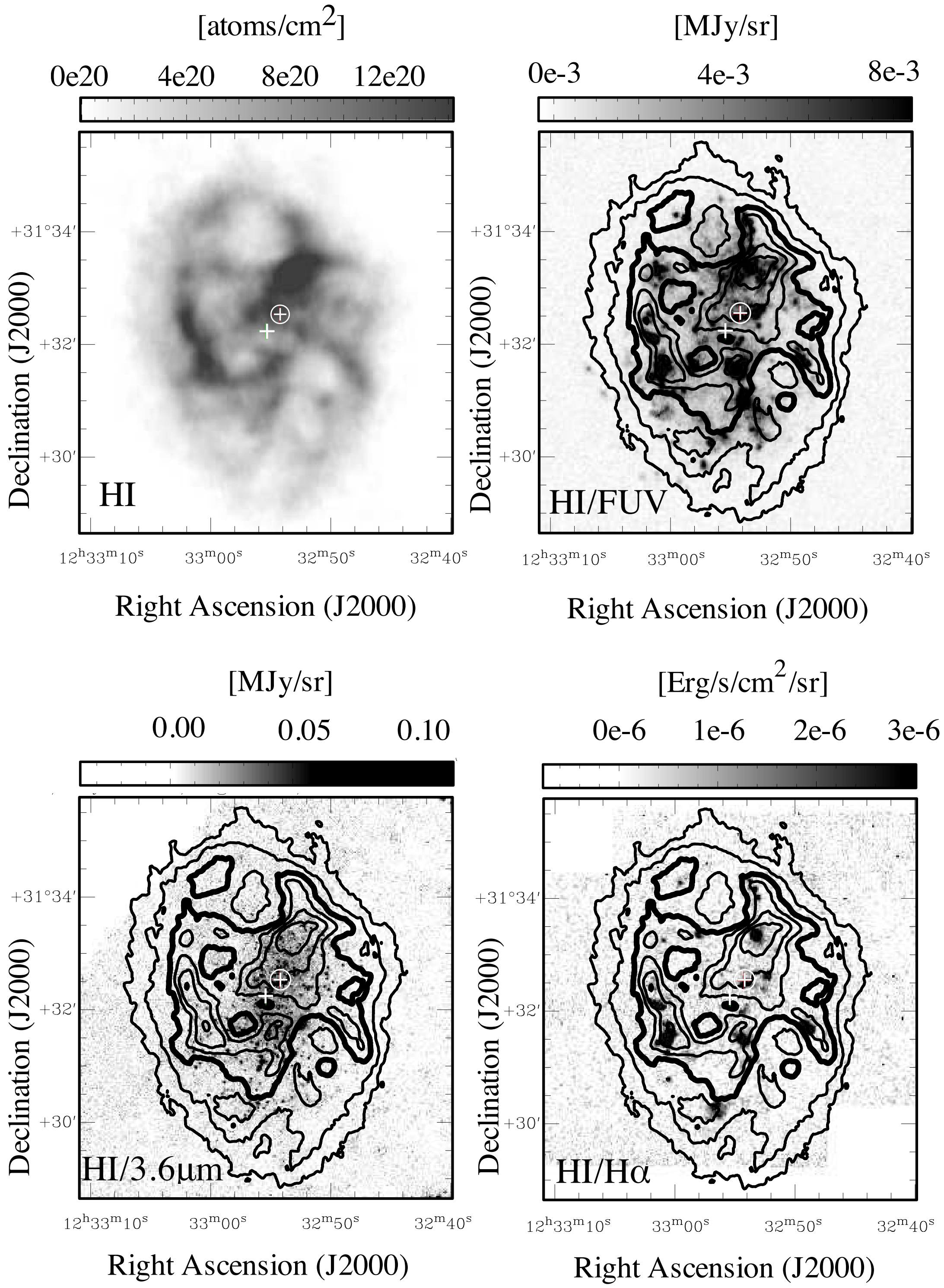

Fig. 3.— DDO 133. Top Left: Integrated H I map (Resolution: 12.4” × 10.8”, lowest confidence level (2.5σ over 3 channels): 0.61×10^{20} atoms cm^{-2}, grey scale: 0 - 1.5×10^{21} atoms cm^{-2}). Top Right: H I contours overlaid on the FUV image (grey scale: 0 - 8×10^{-3} MJy sr^{-1}). Bottom Left: H I contours overlaid on the *Spitzer* 3.6 μm image (grey scale: 0 - 0.2 MJy sr^{-1}). Bottom Right : H I contours overlaid on the Hα map (grey scale: 0 - 1×10^{-7} ergs s^{-1} cm^{-2} sr^{-1}). The H I contours are at (0.1, 0.3, 0.6, 0.9, 1.2, 1.5)1×10^{21} H I atoms cm^{-2}. In all panels the gray plus represents the V–band and the kinematic centre of the galaxy, whereas the gray circled plus represents the centre of the bar.

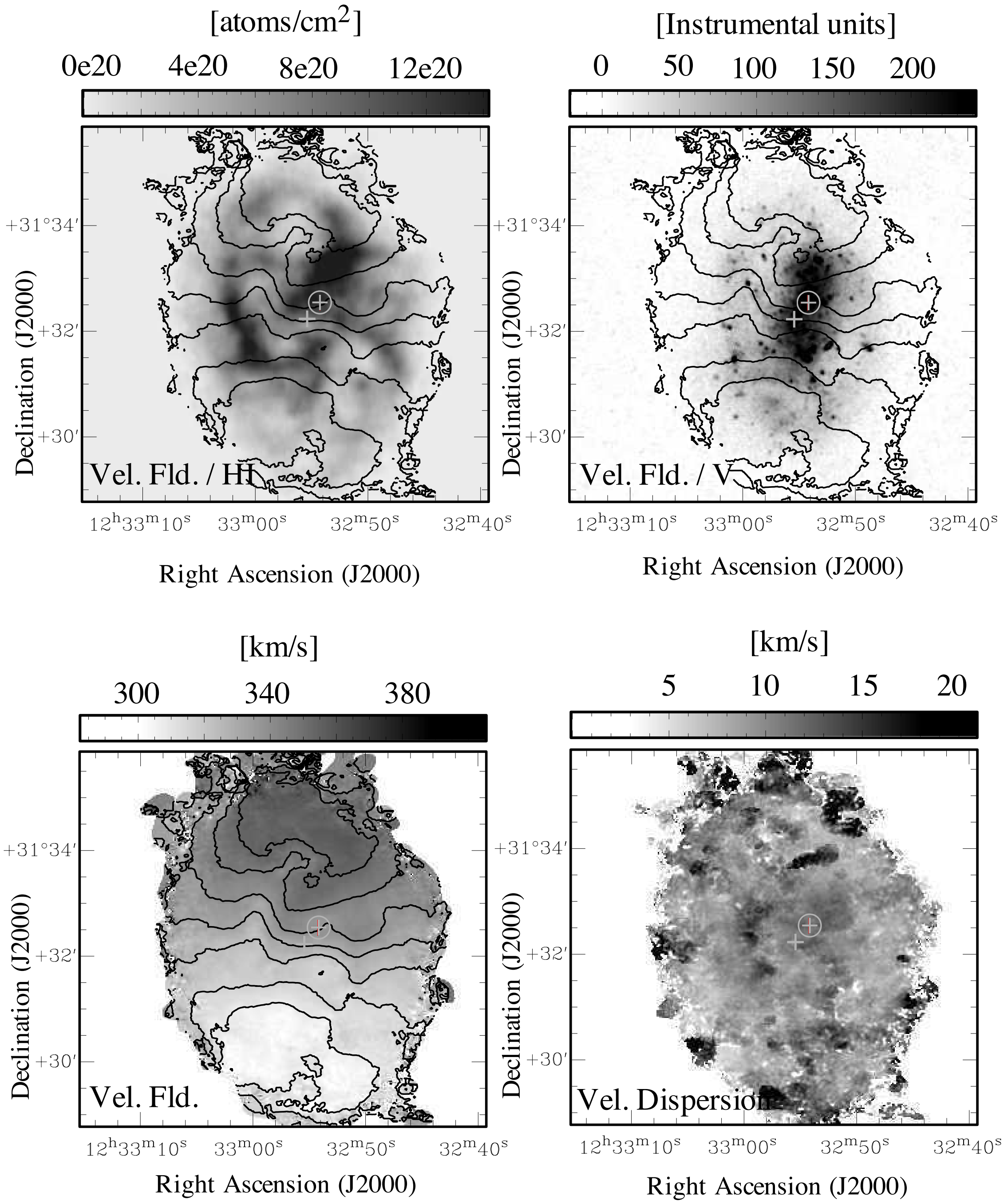

Fig. 4.— DDO 133. Top Left: Integrated H I map (moment 0) with velocity field contours. Top Right: velocity field contours overlaid on the V–band optical image. Bottom Left: Contoured Velocity Field. All iso–velocity contours are spaced by 7 km s^{-1}. Bottom Right : Velocity Dispersion map. In all panels the gray plus represents the V–band and the kinematic centre of the galaxy, whereas the gray circled plus represents the centre of the bar. The blue ellipse delimitates the bar region from the rest of the galaxy.

Table 2. Observing Setup

Name	Array Config.	Observing Date yy-mm-dd	TOS (min)	Secondary Calibrator	BW (MHz)	Han.	Chan. No.
DDO 133	D	04-Jun-21, Aug-21/22	483	1221+282	1.56	Y	128
	C	08-Mar-22, Jun-3	355	1227+365	1.56	N	256
	B	07-Dec-24, 08-Jan-11, Feb-02	520	1227+365	1.56	N	256
DDO 168	D	08-Jul-07	120	1227+365	1.56	N	256
	C	08-Mar-27, Apr-22	355	1227+365	1.56	N	256
	B	08-Jan-20, Feb-01, Feb-06	675	1313+549	1.56	N	256

Table 2: From left to right the columns represent: Galaxy name, Array configuration, Observing Date, Time on source (TOS) in minutes, the secondary Calibrator, Bandwidth in MHz, Hanning smoothing: Y or N, and Number of Channels.

Table 3. Map characteristics

Name	Weighting	Bmaj ($''$)	Bmin ($''$)	BPA ($^\circ$)	Noise (mJy beam^{-1})	Size [pixels]	Pixel ($''$)	Chan.	Width (km s^{-1})
DDO 133	NA	19.17	18.13	-83.95	0.33	1024	1.5	102	2.6
	RO	12.36	10.78	-87.87	0.38				
DDO 168	NA	12.55	11.15	63.21	0.47	1024	1.5	103	2.6
	RO	7.84	5.89	67.49	0.51				

Table 3: From left to right the columns represent: Galaxy name, Weighting function used, Major axis of the synthesized beam in arcseconds, Minor axis of the synthesized beam in arcseconds, Position angle of the synthesized beam in degrees, Noise level in one channel map in mJy beam^{-1}, Size of the map in pixels, Pixel size in arcseconds, Number of channels, and Channel width in km s^{-1}

Table 4: Measured quantities

Name	DDO 133	DDO 168	Notes
$S_{\mathrm{H\,I}}$ (Jy km s^{-1}) *(Single dish)*	40.98 ± 1.6	76.50 ± 4.5	Single dish H I flux from Springob et al. (2005) and Huchtmeier & Richter (1986) respectively
$S_{\mathrm{H\,I}}$ (Jy km s^{-1}) *(Observed)*	36.42	64.00	LITTLE THINGS H I Flux
log ($M_{\mathrm{H\,I}}$) (log($M_{\odot}$)) *(Literature)*	8.09	8.51	H I mass from Fisher & Tully (1981) and Hunter & Gallagher (1985) respectively
log ($M_{\mathrm{H\,I}}$) (log($M_{\odot}$)) *(Observed)*	8.02	8.45	LITTLE THINGS H I mass
log (M_{H2}) (log($M_{\odot}$)) *(Predicted)*	7.03	7.26	Predicted H_2 mass
W_{20} (km s^{-1})	83	87	Profile width at 20% of the peak intensity
v_{rot} (km s^{-1})	40 ± 5	50 ± 7	Kinematically determined rotational velocity
Incl. (°)	47 ± 5	55 ± 8	Inclination determined from kinematical studies

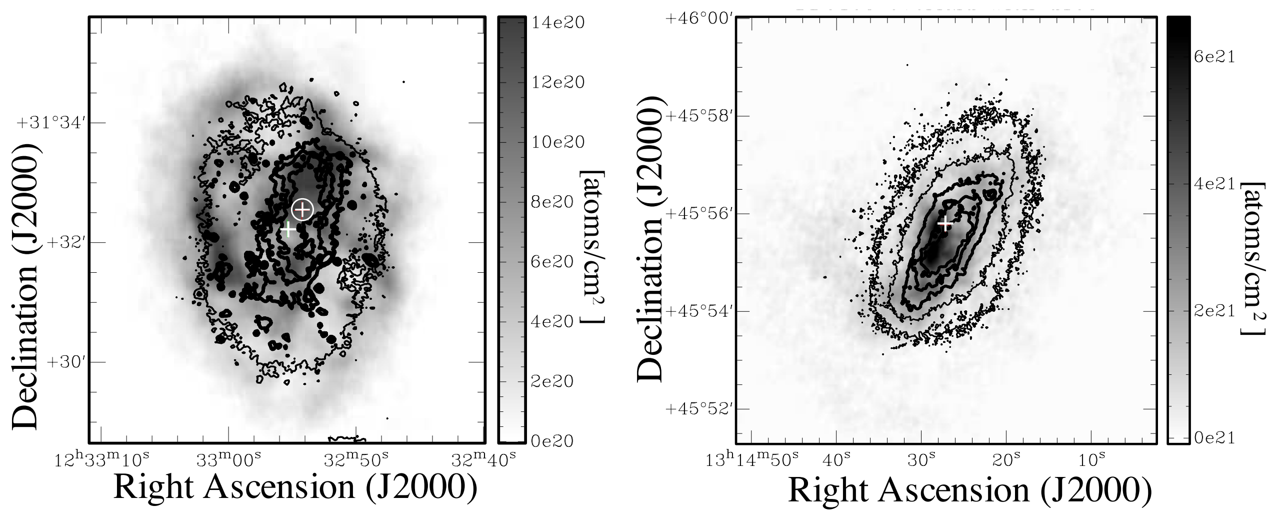

Fig. 5.— DDO 133 (left) and DDO 168 (right): Integrated H I map (moment 0) with optical V–band contours. The V–band contours are at (25.8, 24.6, 24.2, 23.9) mag arcsec^{-2} for DDO 133 and at (25.9, 25.0, 24.0, 23.3, 22.8) mag arcsec^{-2} for DDO 168.

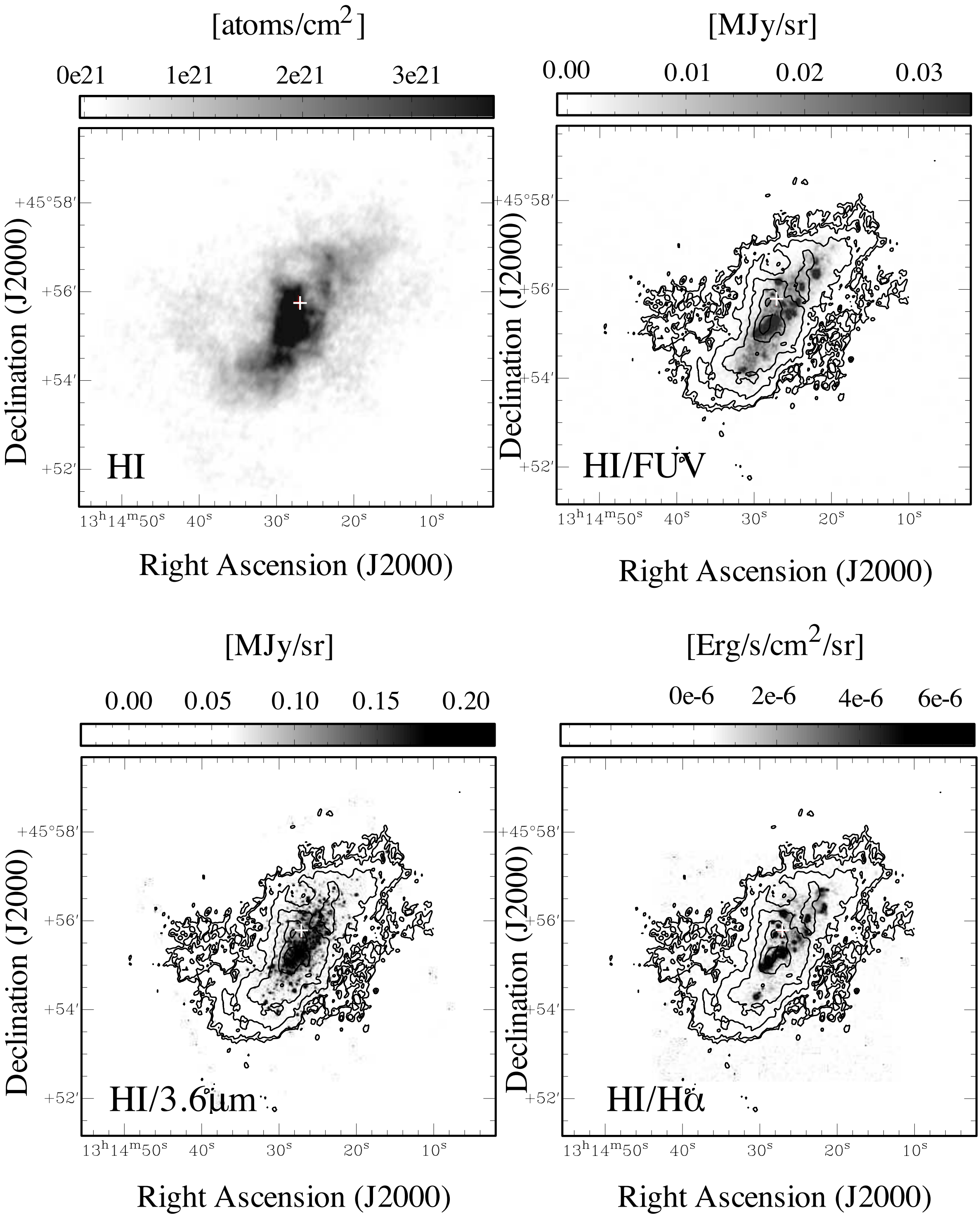

Fig. 6.— DDO 168. Top Left: Integrated H I map (Resolution: 7.8” × 5.8”, lowest confidence level (2.5σ over 3 channels): 2.4×10^{20} atoms cm^{-2}, grey scale: 0 - 6×10^{21} atoms cm^{-2}). Top Right: H I contours overlaid on the FUV image (grey scale: 0 - 3×10^{-2} MJy sr^{-1}). Bottom Left: H I contours overlaid on the *Spitzer* 3.6 μm image (grey scale: 0 - 0.2 MJy sr^{-1}). Bottom Right : H I contours overlaid on the Hα map (grey scale: 0 - 6×10^{-6} ergs s^{-1} cm^{-2} sr^{-1}). The H I contours are at (0.35, 0.5, 1, 2, 4, 6)$\times10^{21}$ H I atoms cm^{-2}. In all panels the gray plus represents the kinematic and the V–band centre of the galaxy.

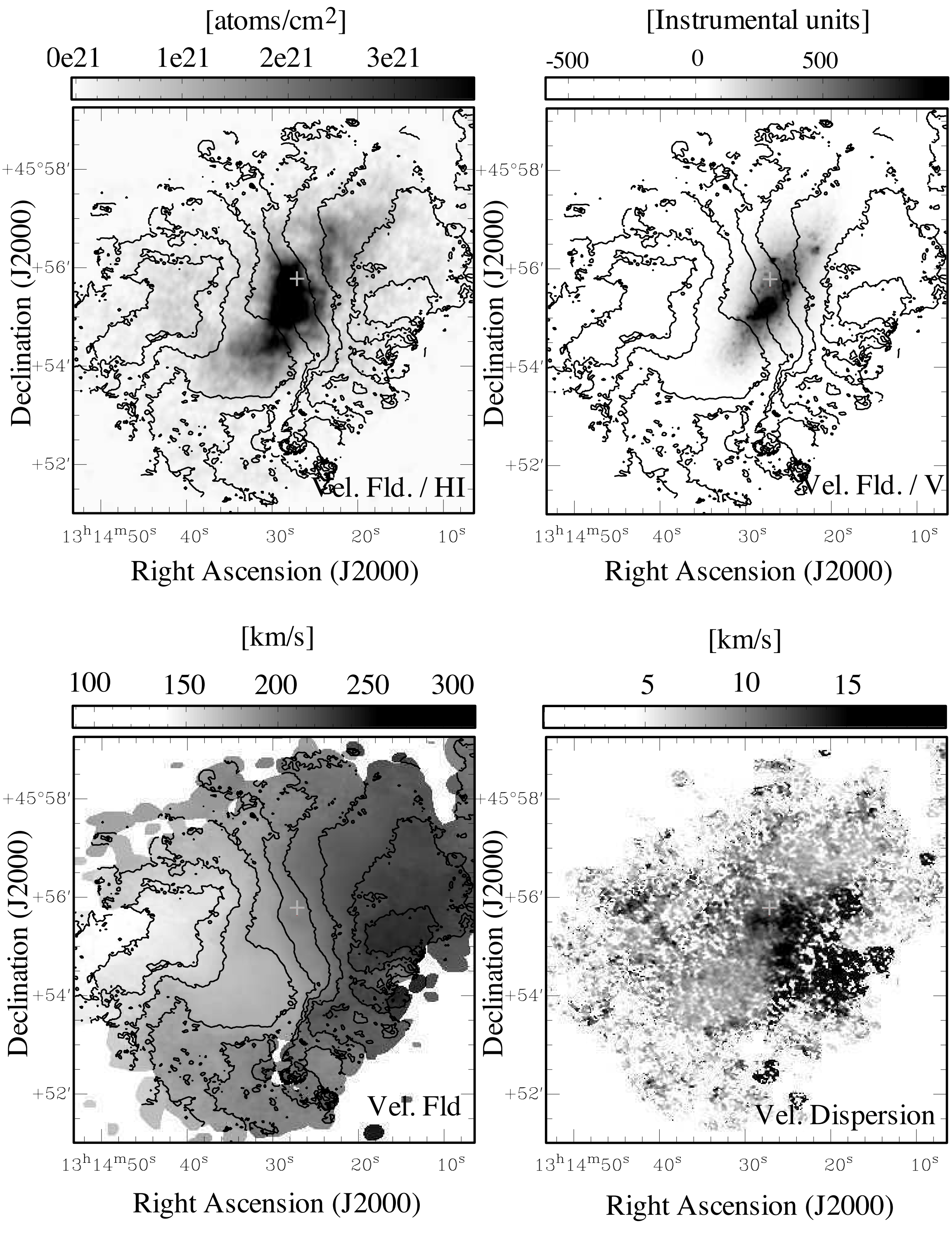

Fig. 7.— DDO 168. Top Left: Integrated H I map (moment 0) with velocity field contours. Top Right: velocity field contours overlaid on the V–band optical image. Bottom Left: Contoured Velocity Field. All iso–velocity contours are spaced by 10 km s^{-1}. Bottom Right : Velocity Dispersion map. In all panels the gray plus represents the kinematic and the V–band centre of the galaxy.

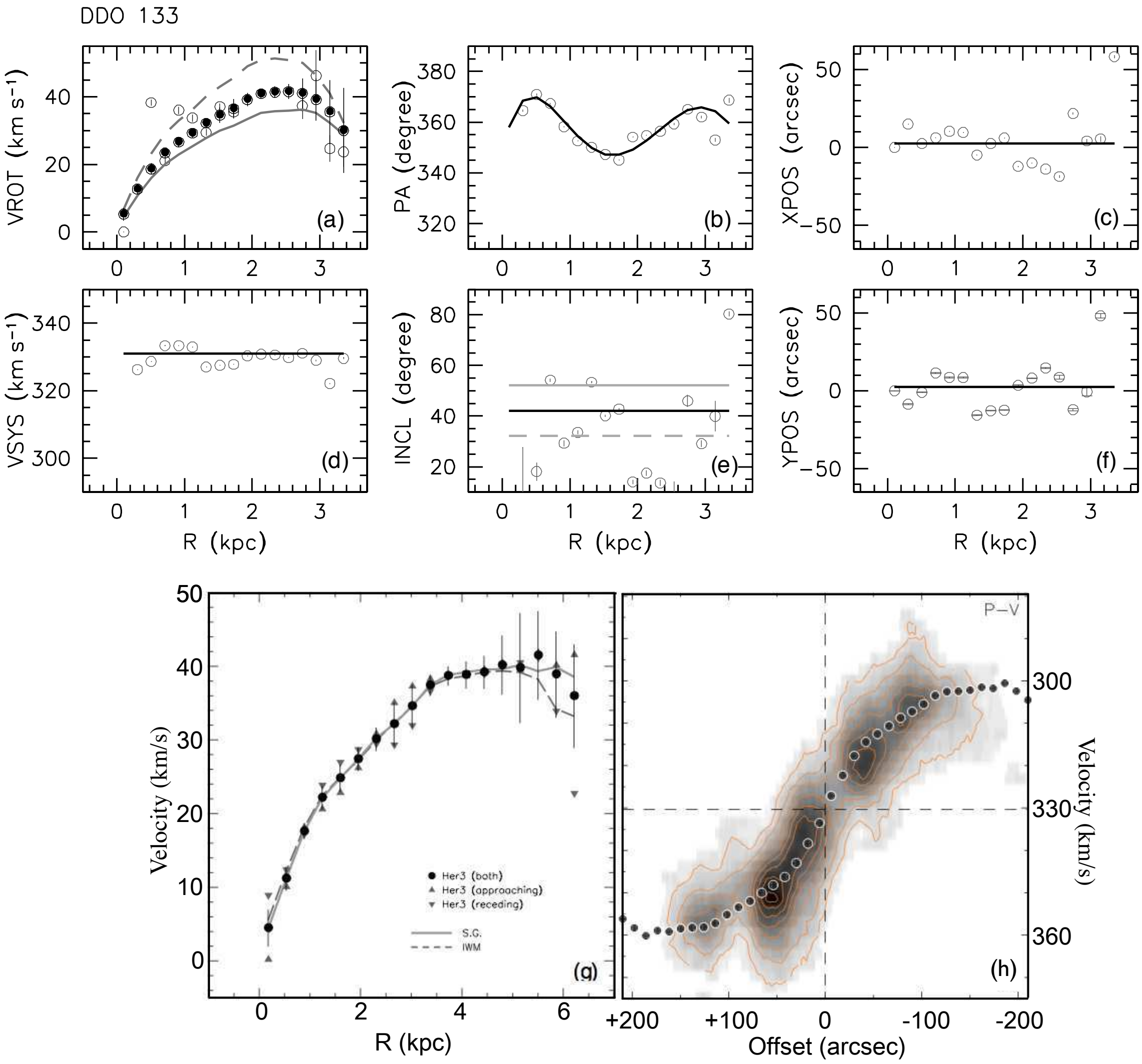

Fig. 8.— Summary of the kinematical study results for DDO 133: (a) — Rotational velocity, (b) — Position angle, (c) — Position of the kinematic centre on the X axis, (d) — Systemic velocity, (e) — Inclination, (f) — Position of the kinematic centre on the Y axis, (g) — Rotation curve fitting and (h) – Rotation curve overimposed on the position–velocity diagram. The black solid lines represent the tilted–ring parameters that best describe the velocity fields considered. Open circles trace the results derived from keeping all parameters free. In (g) panel we show three rotation curves derived using the different velocity fields : IWM — dashed grey line, single Gaussian function — continuous grey line and Gauss–Hermite h_3 polynomial — black filled circles line.

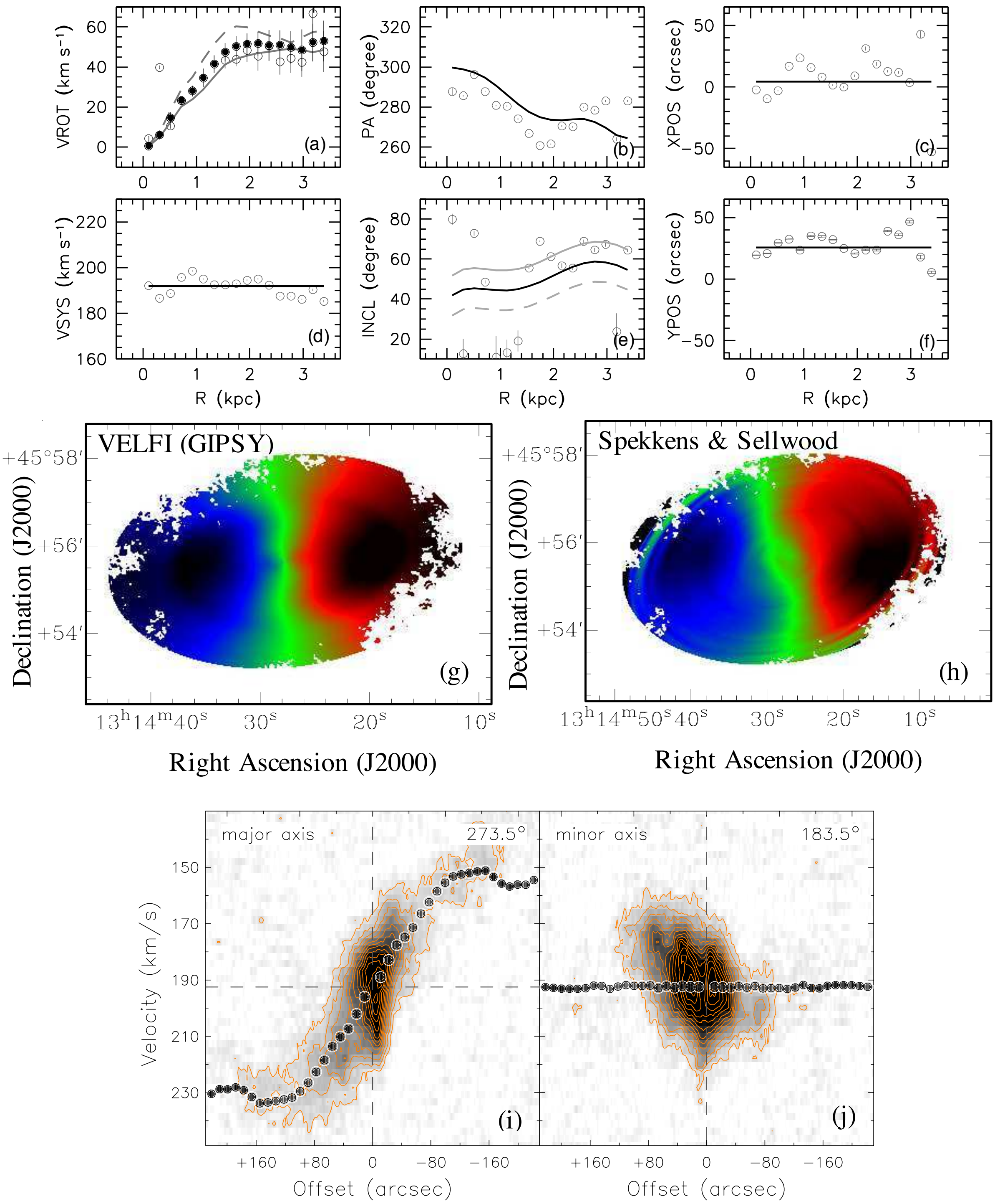

Fig. 9.— Summary of the kinematical study results for DDO 168: (a) — Rotational velocity, (b) — Position angle, (c) — Position of the kinematic centre on the X axis, (d) — Systemic velocity, (e) — Inclination, (f) — Position of the kinematic centre on the Y axis, (g) — Standard VELFI (GIPSY) model velocity field, (h) — Spekkens & Sellwood (2007) (VELFIT) model velocity field, (i) – Rotation curve overimposed on the position–velocity diagram along the major axis, and (j) – Rotation curve overimposed on the position–velocity diagram along the minor axis.

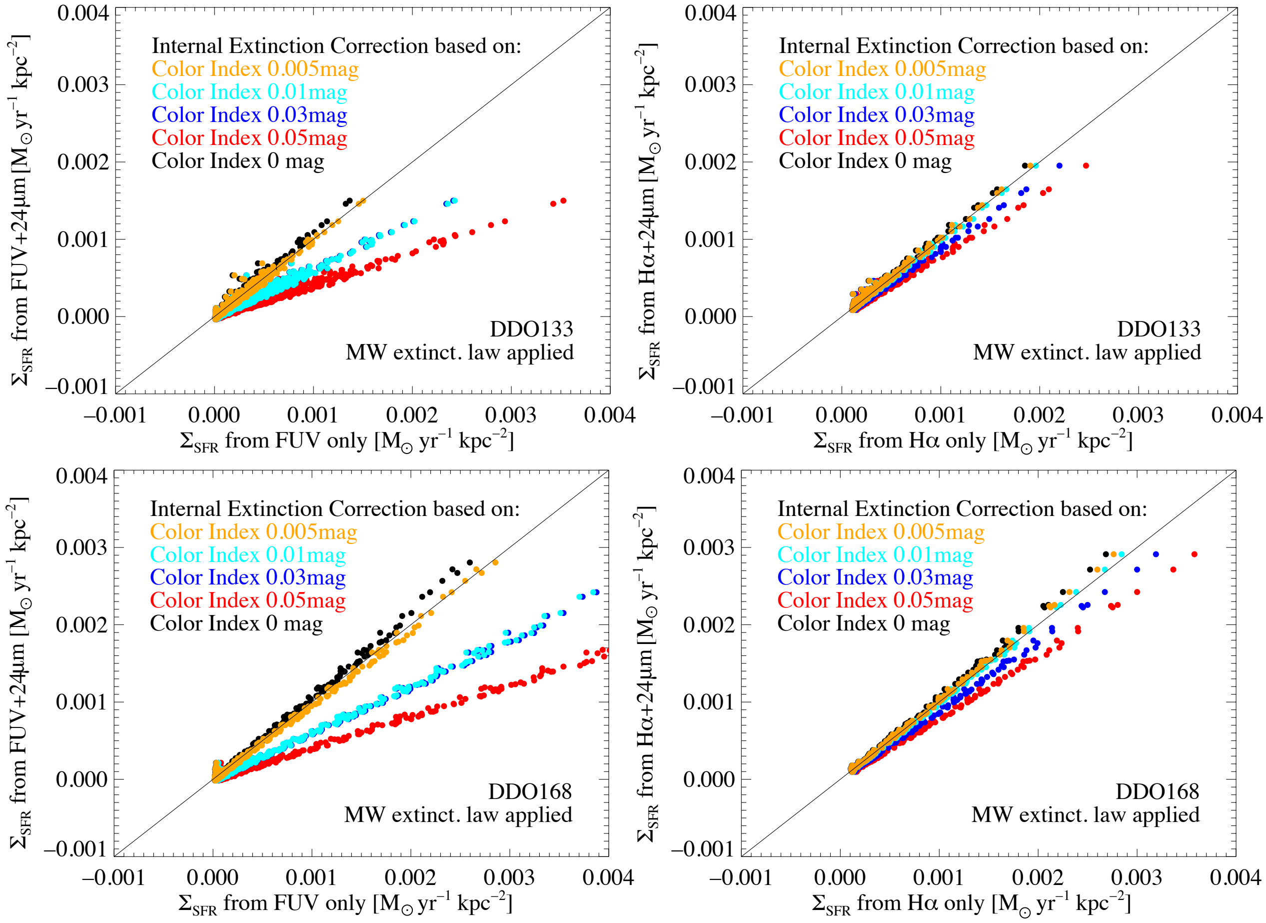

Fig. 10.— DDO 133 (top) and DDO 168 (bottom), we present SFR surface density derived from FUV only vs. SFR surface density based on FUV+24 μm (right) and SFR surface density from Hα only vs SFR surface density based on Hα+24 μm (left). Different colours represent internal extinction corrections of different colour index numbers: 0.05 mag (red), 0.03 mag (blue), 0.01 mag (cyan), 0.005 mag (orange) and 0 mag (black). The black continuous line represents a 1:1 relation between the x and y axis.

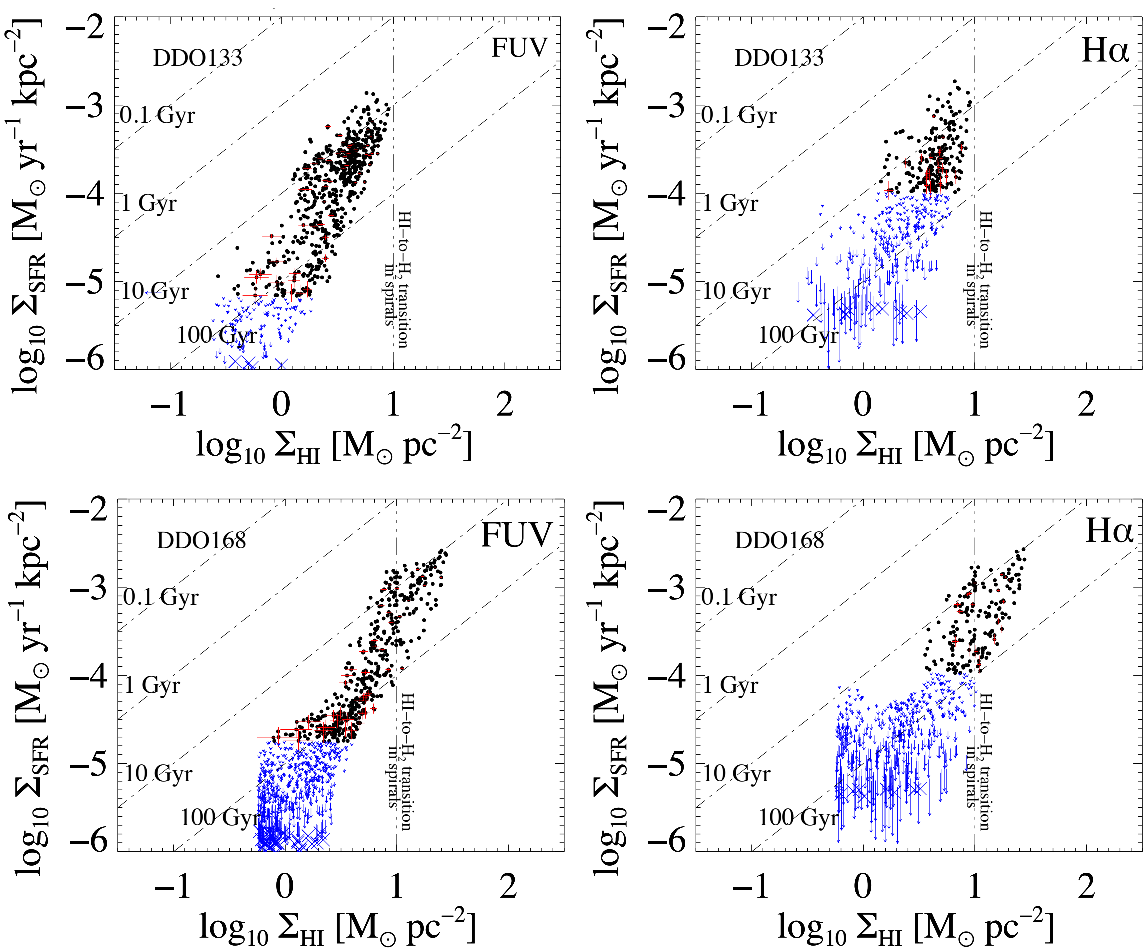

Fig. 11.— DDO 133 (top) and DDO 168 (bottom), we present SFR surface density derived from FUV only (left) and Hα only (right) vs. H I surface density. All points are independent and above a 5σ cutoff level. In red we display error bars for every $10^{\rm th}$ point in the plot. With blue arrows we represent the upper limits. The vertical dashed line represents an H I surface density of $10\,M_\odot$ pc^{-2}. The other three dashed lines represent constant depletion times of 0.1 Gyr, 1 Gyr , 10 Gyr and 100 Gyr.

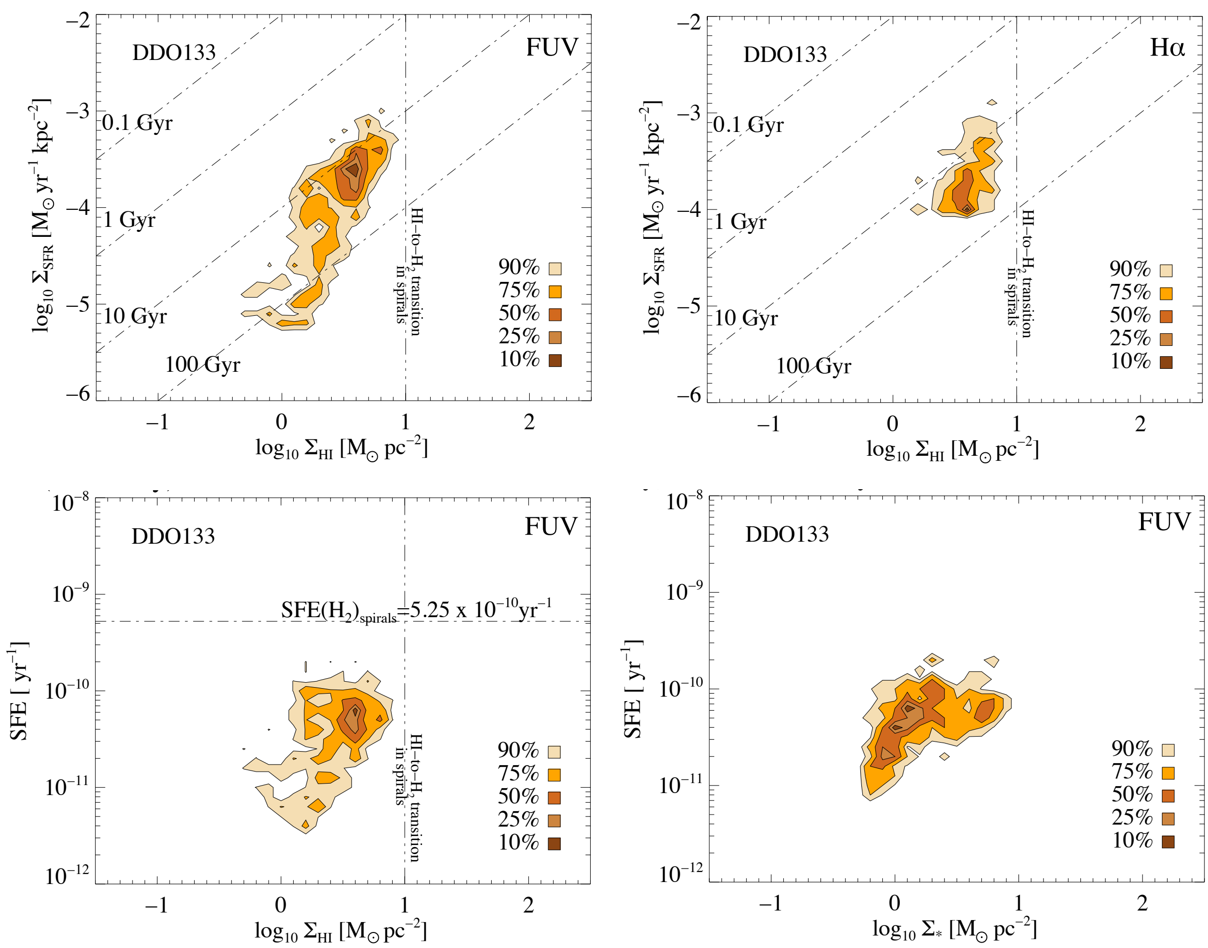

Fig. 12.— DDO 133. Density contours at 10%, 25%, 50%, 75% and 90% of the pixel by pixel distribution of: SFR surface density vs. H I surface density plotted separately for two different SF tracers FUV (top left) and Hα (top right) and SFE vs H I surface density (bottom left) and vs stellar surface density (based on the 3.6 μm *Spitzer* map) for FUV as an SF tracer (bottom right). All maps used for the above plots have the same linear resolution of 400 pc. All points are independent and above a 5σ cutoff level. The vertical dashed line represents an H I surface density of 10 $M_\odot$ pc^{-2}. The horizontal dashed line represents constant molecular gas SFE of 5.25×10^{-10} yr^{-1}. The other three dashed lines in the top row represent constant depletion times of 0.1 Gyr, 1 Gyr, 10 Gyr and 100 Gyr.

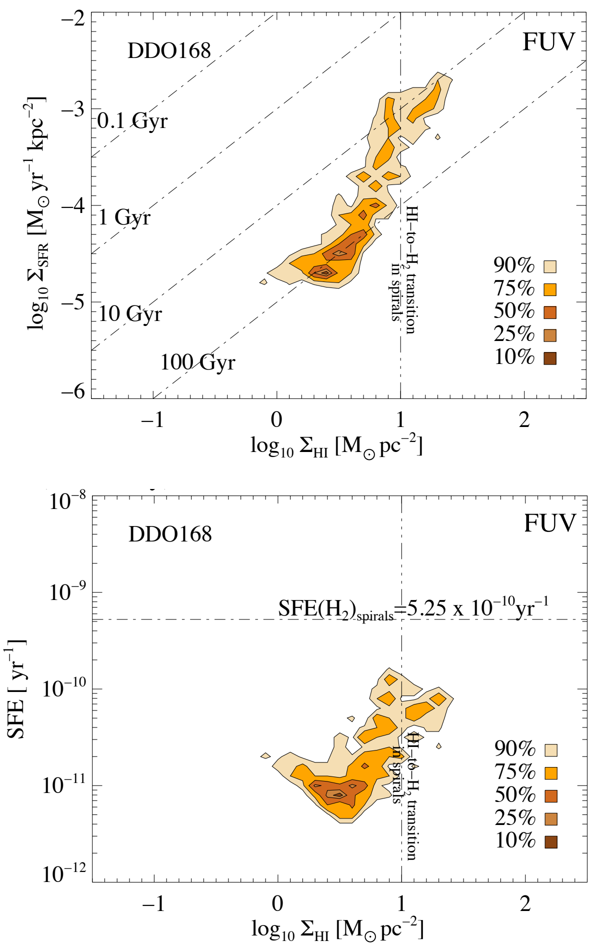

Fig. 13.— DDO 168. Density contours at 10%, 25%, 50%, 75% and 90% of the pixel by pixel distribution of: SFR surface density vs. H I surface density plotted separately for two different SF tracers FUV (top left) and Hα (top right) and SFE vs H I surface density (bottom left) and vs stellar surface density (based on the 3.6 μm *Spitzer* map) for FUV as an SF tracer (bottom right). All maps used for the above plots have the same linear resolution of 400 pc. All points are independent and above a 5σ cutoff level. The vertical dashed line represents an H I surface density of 10 M$_\odot$ pc^{-2}. The horizontal dashed line represents constant molecular gas SFE of 5.25×10^{-10} yr^{-1}. The other three dashed lines in the top row represent constant depletion times of 0.1 Gyr, 1 Gyr, 10 Gyr and 100 Gyr.

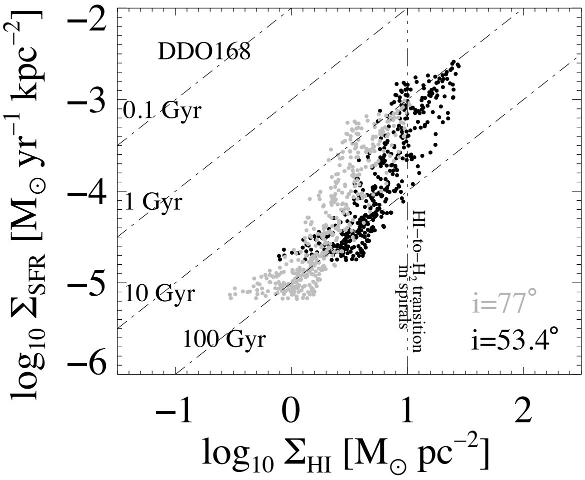

Fig. 14.— The effect of different inclination corrections applied to the SFR surface density vs. H I surface density plot. Red points are corrected for an inclination of 77 °, whereas the blue points are corrected for an inclination of 55 °. The three dashed lines represent constant depletion times of 0.1 Gyr, 1 Gyr, 10 Gyr and 100 Gyr.

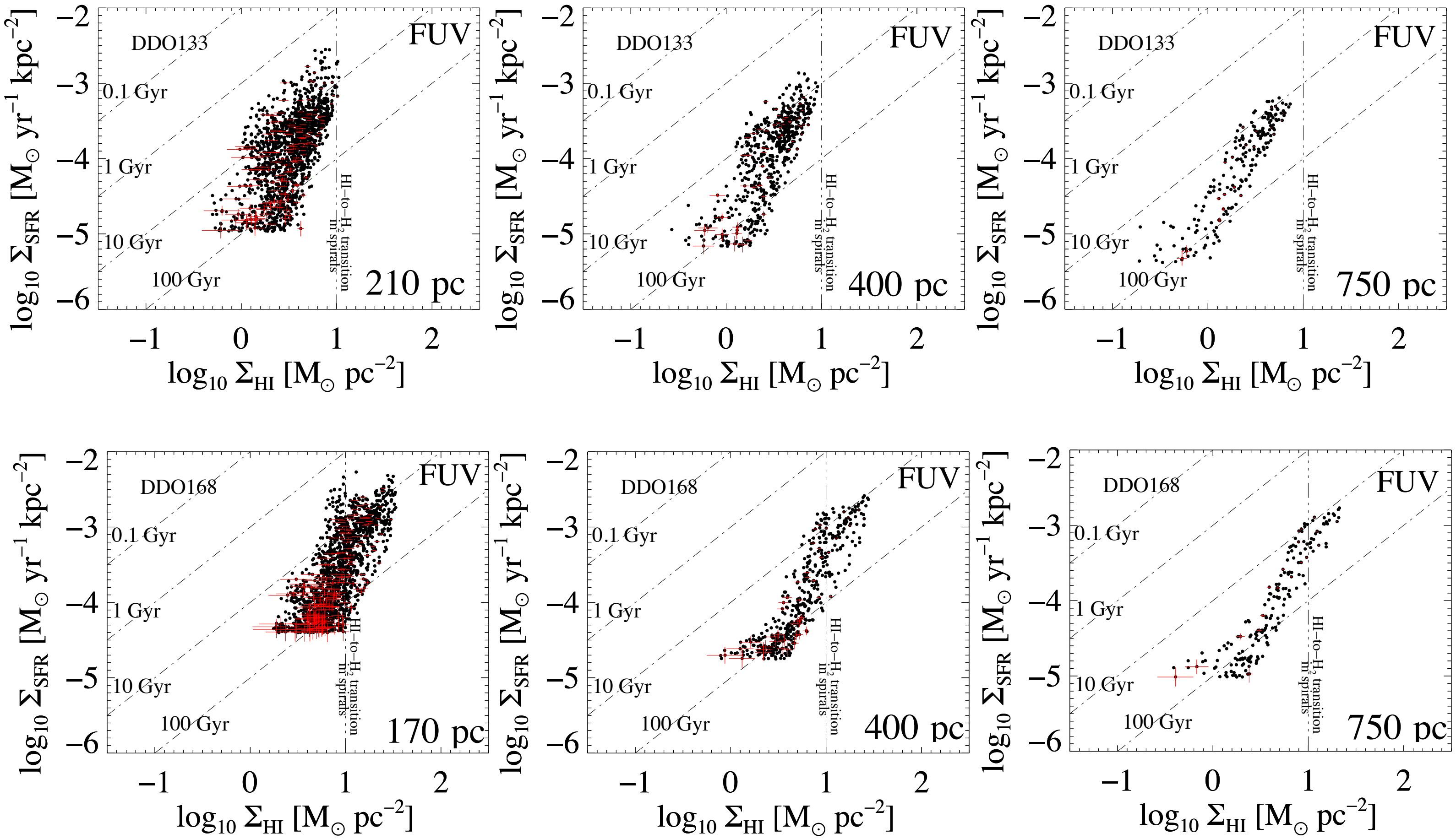

Fig. 15.— DDO 133 on the top row and DDO 168 on the bottom row, from left to right we show SFR surface density vs. H I surface density using three different resolutions: the finest linear resolution (210 pc for DDO 133 and 170 pc for DDO 168), 400 pc linear resolution and 750 pc linear resolution. The SFR surface density has is based on FUV only as a star formation tracer. All points are independent and above a 5σ cutoff level. In red we display error bars for every 10^{th} point in the plot. The vertical dashed line represents an H I surface density of $10\,\mathrm{M_\odot\,pc^{-2}}$. The other three dashed lines represent constant depletion times of 0.1 Gyr, 1 Gyr, 10 Gyr and 100 Gyr.

Appendix A

Maps

We present here the H I channel maps of DDO 133 and DDO 168 in Fig. A1 and Fig. A2. These channel maps are based on the robust cubes and the noise levels of these cubes are: σ= 1.7 K for DDO 133 and σ= 6.8 K for DDO 168. Note that the beam sizes (12.4" $\times$ 10.8" for DDO 133 and 7.8" $\times$ 5.8" for DDO 168) are indicated in the bottom left corner of the top left panel, however they may be too small to be properly reproduced. All emission channels are shown. In the top right of each panel is indicated the heliocentric radial velocity of the H I gas in km s^{-1}.

At the first glance we see in the channel maps of DDO 133 a galaxy with extended gas structure, in symmetrical rotation and with an abundance of H I holes. In DDO 168 the H I distribution is more compact and clumpy.

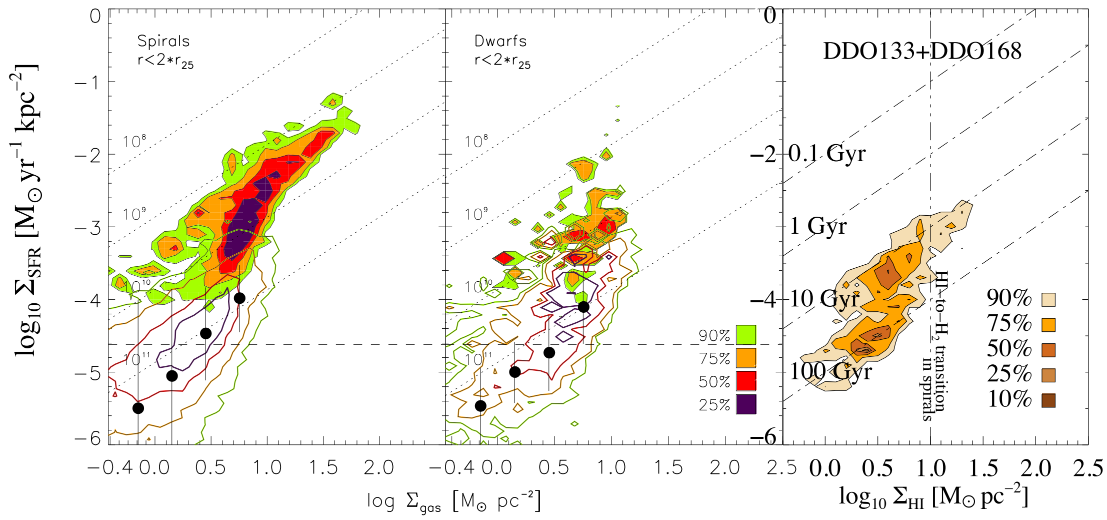

Fig. 16.— First two panels, one for THINGS spirals and the other for THINGS dwarfs summarise the results of Bigiel et al. (2010). The filled colour contours show the pixel by pixel distribution of FUV converted to SFR surface density as a function of gas surface density inside r_{25}, whereas the empty contours show the same thing but outside r_{25}. The horizontal dashed line indicates the 3σ sensitivity level of the FUV measurement. The black filled circles represent their best fit through the data. In the last panel we attached our results for comparison: density contours at 10%, 25%, 50%, 75% and 90% of the pixel by pixel distribution of log SFR surface density vs. log H I surface density of DDO 133 and DDO 168. All points are independent and above a 5σ cutoff level. The vertical dashed line represents an H I surface density of 10 $M_\odot$ pc^{-2}. In all three panels the four dashed lines represent constant depletion times of 0.1 Gyr, 1 Gyr, 10 Gyr and 100 Gyr.

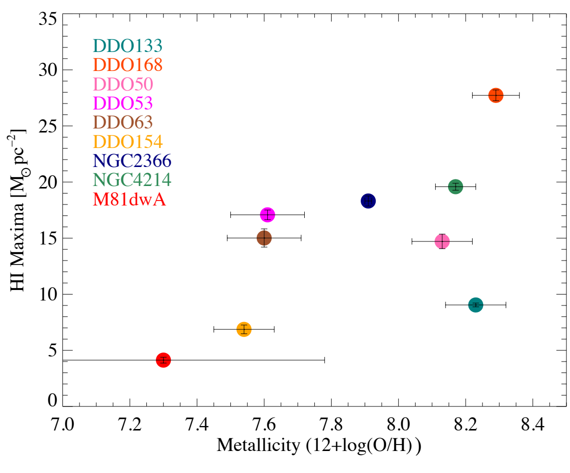

Fig. 17.— Metallicity vs. H I Maxima for DDO 133, DDO 168 and the THINGS dwarf sample (DDO 50, DDO 53, DDO 63, DDO 154, NGC 2366, NGC 4214, M81dwA). The metallicity values and error bars are taken from Hunter et al. (2012), as the above mentioned THINGS dwarfs are also part of the LITTLE THINGS sample.

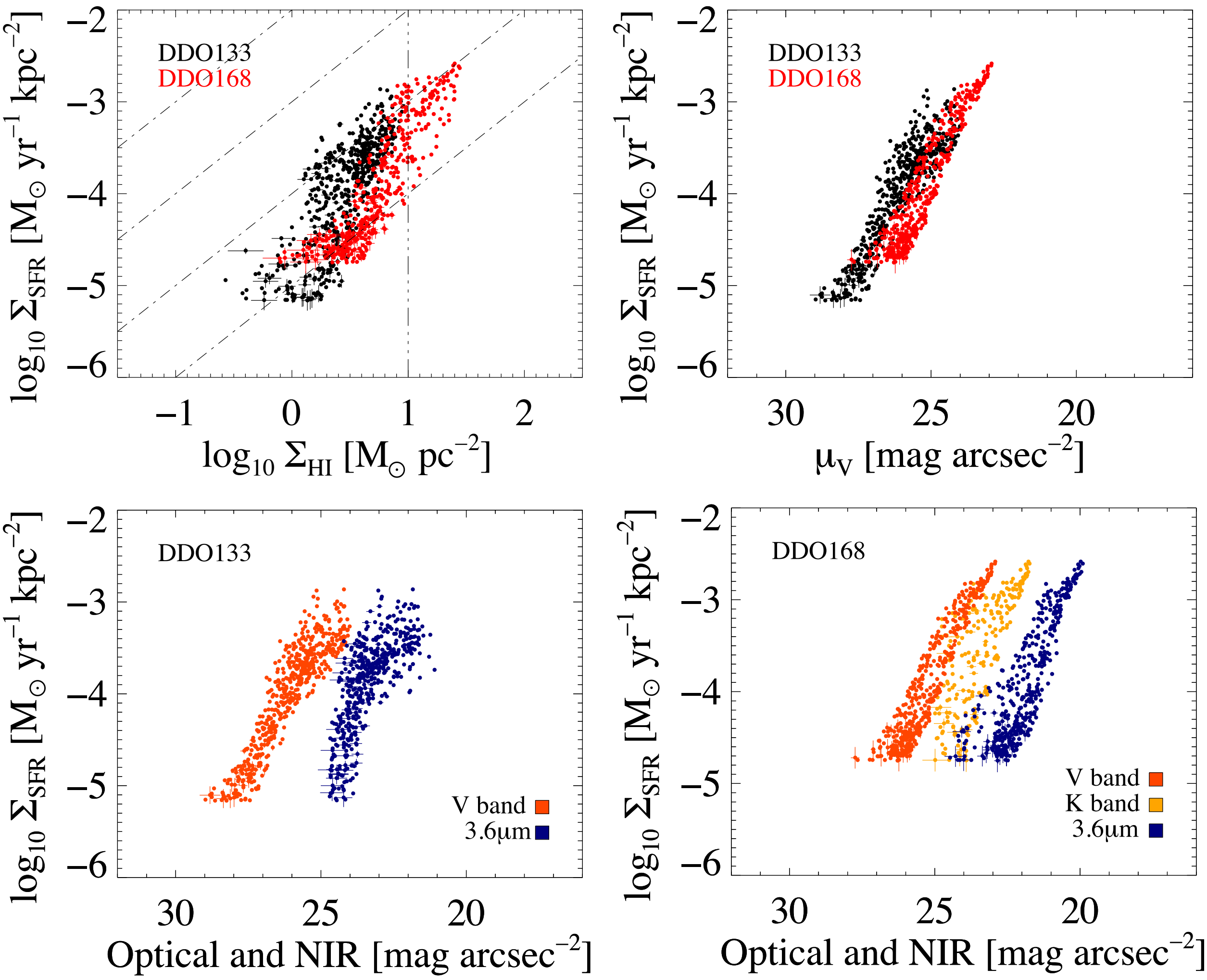

Fig. 18.— Log SFR surface density vs. log of 3.6 μm map (left), K–band emission (middle) and V–band emission (right) of DDO 133 (black triangles) and DDO 168 (red diamonds). All points are independent and above a 5σ cutoff level. In red (for DDO 168) and black (for DDO 133) we also display error bars for every 10^{th} point in the plot.

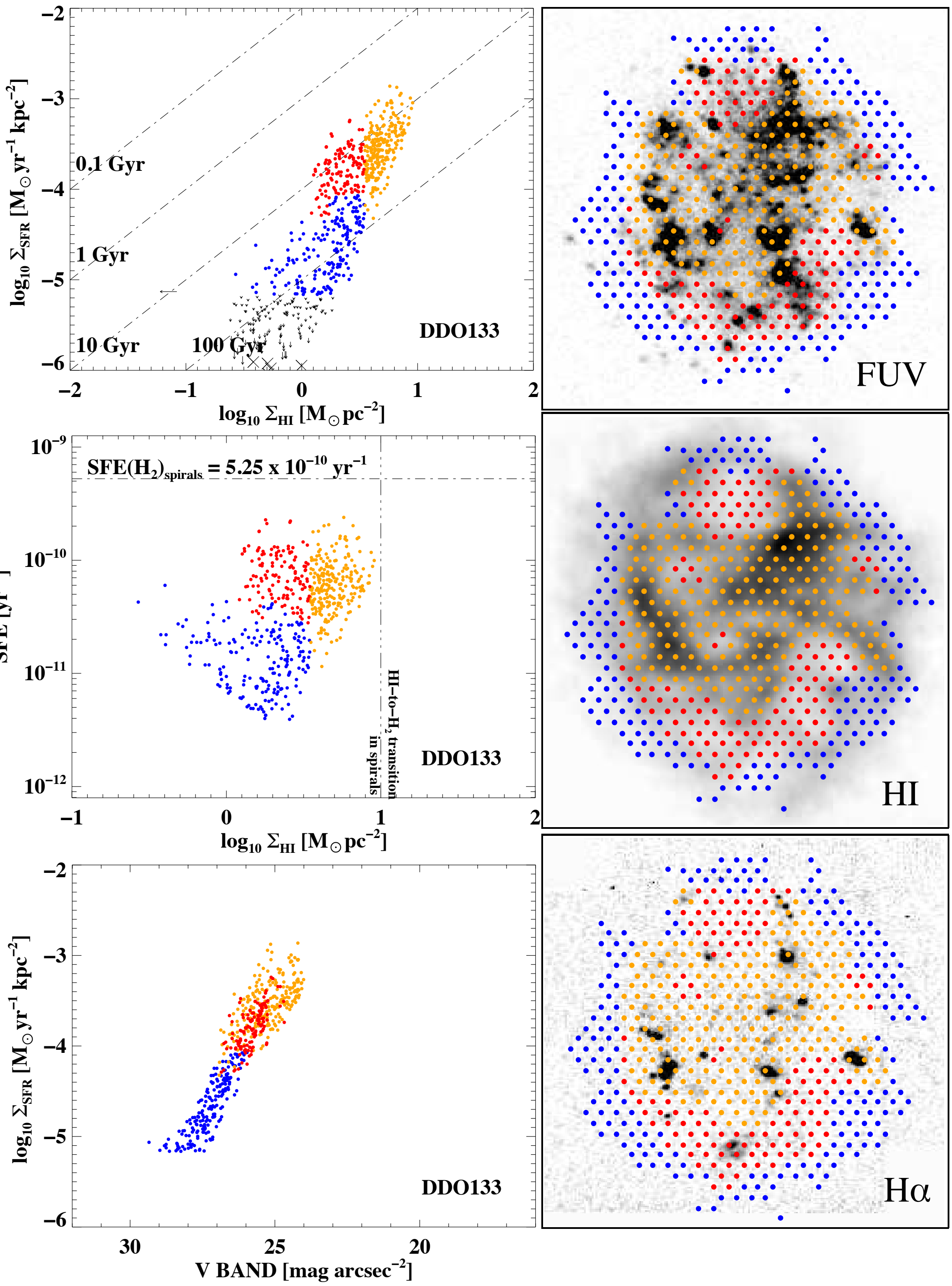

Fig. 19.— DDO 133: Based on the H I distribution map we separate three components in the SF Law and plot their position in the FUV (top right), H I (middle right) and Hα(bottom right) maps. We also plot the same points as above in a SFR plot and a SFE vs H I surface density plots (middle left) and SFR surface density vs. V band emission (bottom left). The vertical dashed line represents an H I surface density of $10\,M_\odot\,pc^{-2}$. The horizontal dashed line represents constant molecular gas SFE of $5.25\times10^{-10}\,yr^{-1}$. The other three dashed lines in the top left panel represent constant depletion times of 0.1 Gyr, 1 Gyr, 10 Gyr and 100 Gyr.

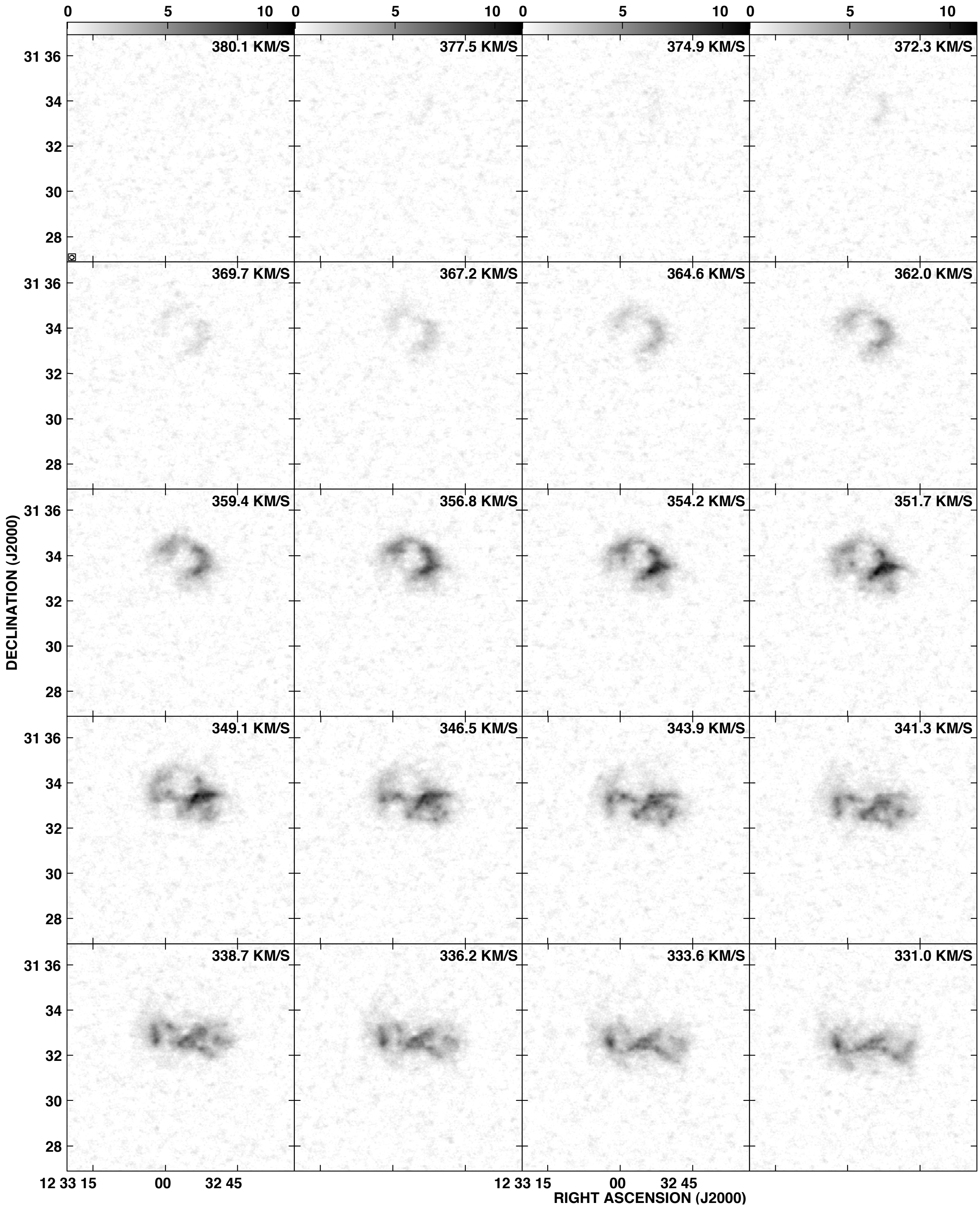

Fig. A1.— DDO 133. Channel maps based on the robust weighted cube (Resolution: 12.4” × 10.8”, σ= 1.7 K) . The grey scale range is: 0-51.6 K (0 - 11.3 mJy/BEAM). First half of all emission channels are shown. The beam is indicated in the bottom left corner of the top left panel.

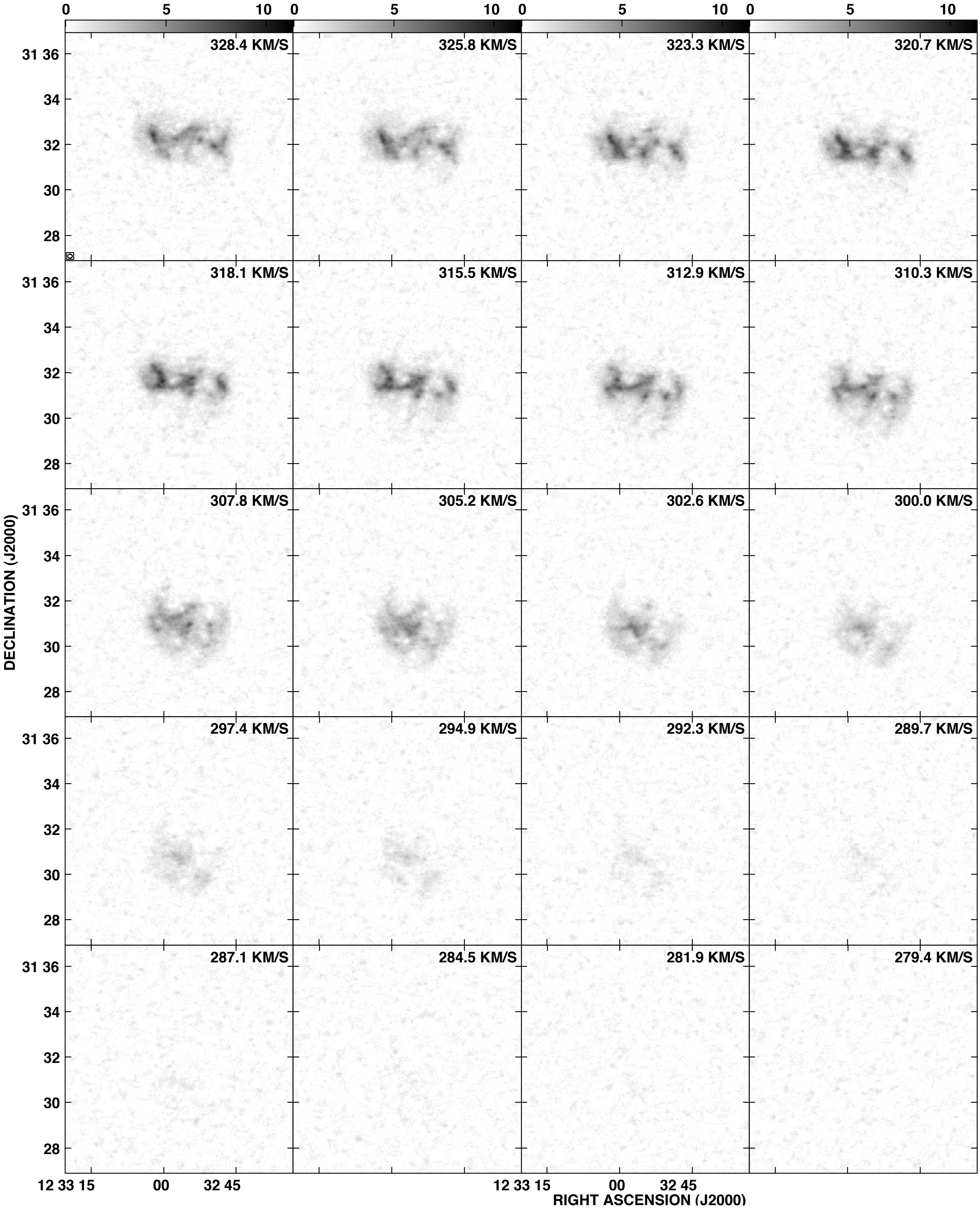

Fig. A1.— (continued)

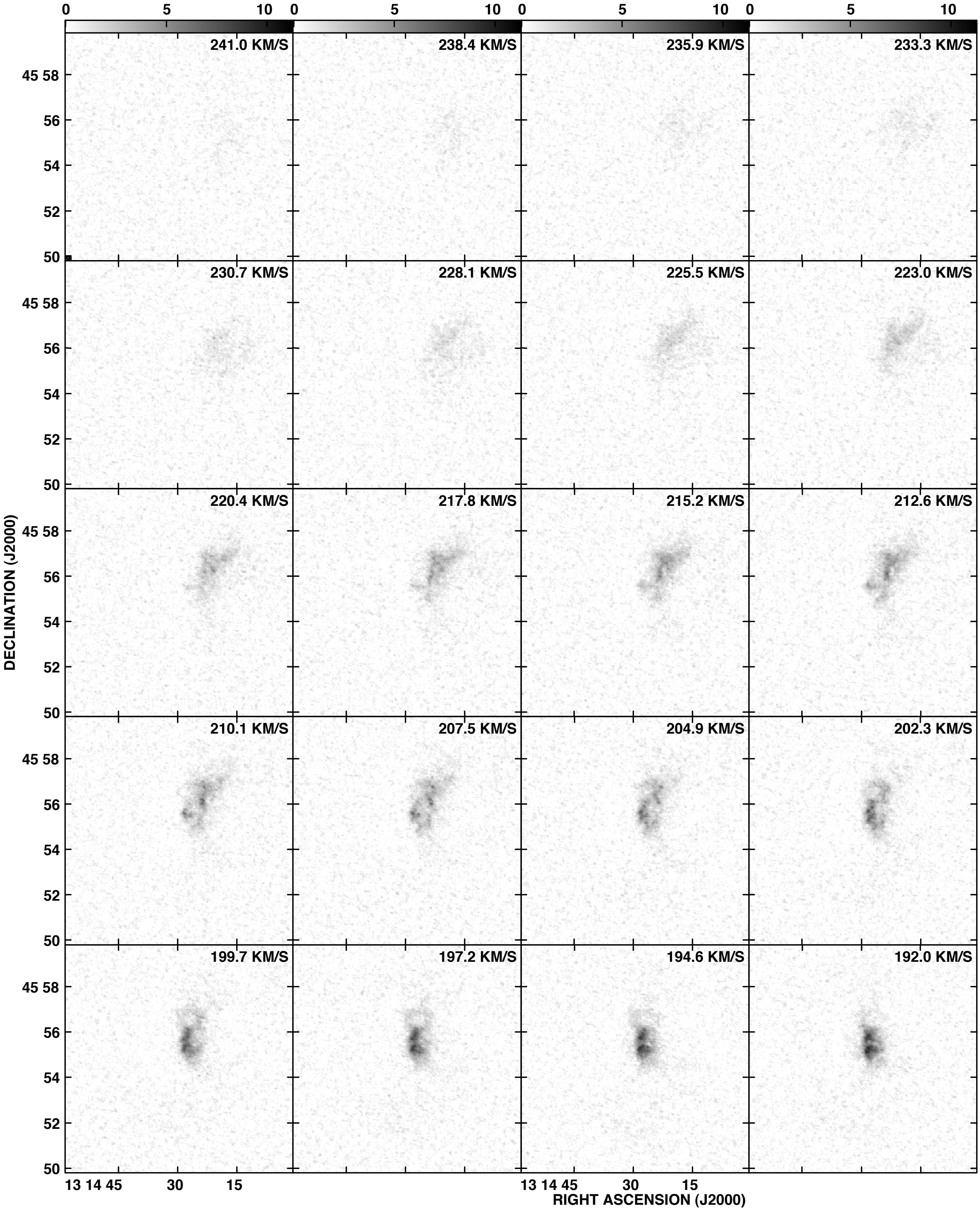

Fig. A2.— DDO 168. Channel maps based on the robust weighted cube (Resolution: 7.8" × 5.8", σ= 6.8 K) . The grey scale range is: 0-150.3 K (0 - 11.3 mJy/BEAM). First half of all emission channels are shown. The beam is indicated in the bottom left corner of the top left panel.

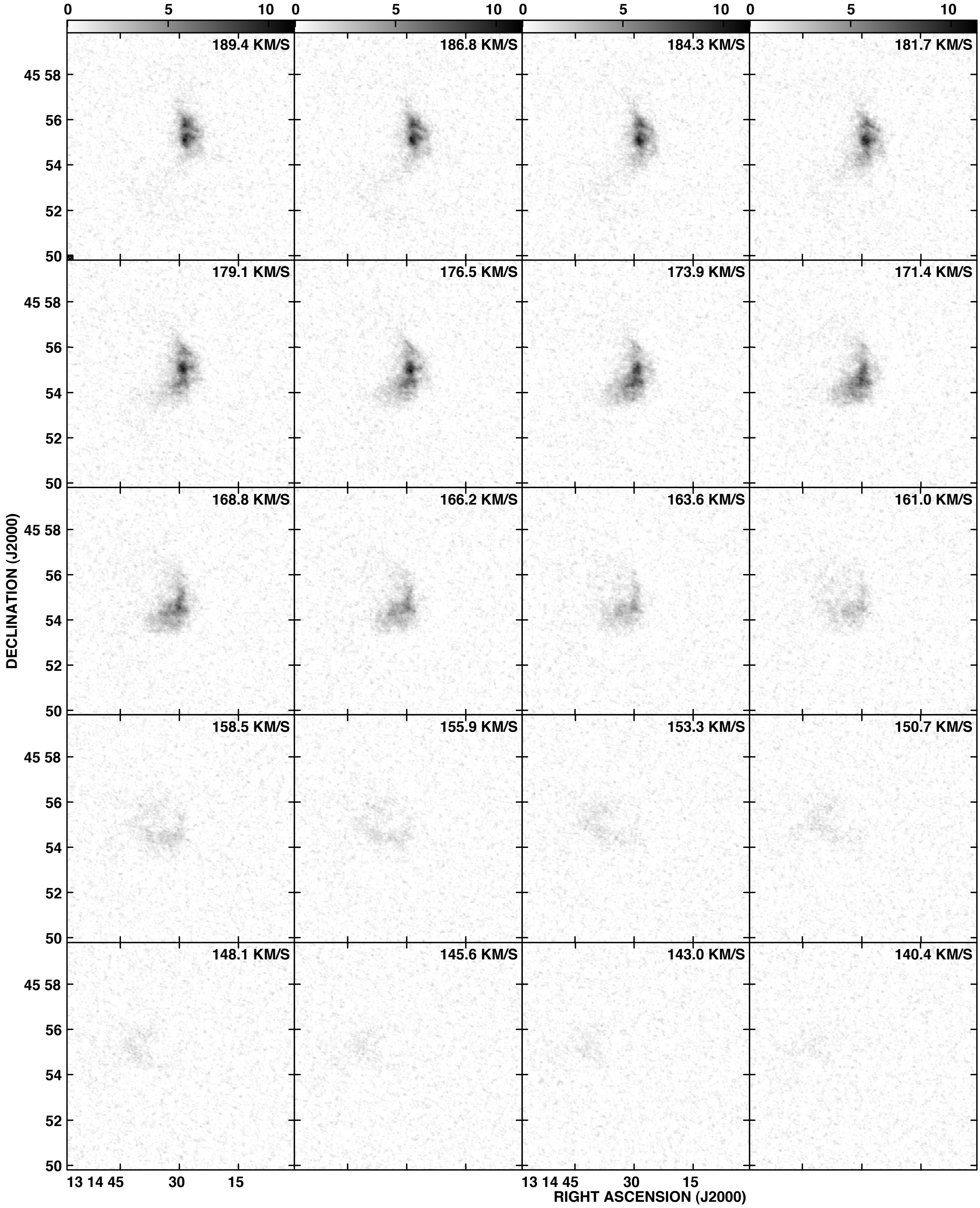

Fig. A2.— (continued)